Development of Gold/Gold Sulfide Nanoparticles for Photothermal and Photodynamic Therapy

by

Dilara Sipahioğlu

A Dissertation Submitted to the
Graduate School of Sciences and Engineering
in Partial Fulfillment of the Requirements for
the Degree of

Master of Science

in

Chemistry

September 5, 2023

Development of Gold/gold Sulfide Nanoparticles for Photothermal and Photodynamic Gas Therapy

Koç University

Graduate School of Sciences and Engineering

This is to certify that I have examined this copy of a master's thesis by

Dilara Sipahioğlu

and have found that it is complete and satisfactory in all respects,
and that any and all revisions required by the final
examining committee has been made.

Committee Members:

_____

Prof. Havva Yağcı Acar

_____

Prof. Mehmet Burçin Ünlü

_____

Assoc. Prof. Safacan Kölemen

Date: 5.09.2023

Dedicated to my family and bellowed ones.

ABSTRACT

Development of Gold/Gold Sulfide Nanoparticles for Photothermal and Photodynamic Therapy

Dilara Sipahioğlu

Master of Science in Chemistry

September 5, 2023

Cancer is a high-mortality disease. There is an urgent need for alternative or adjuvant therapies with high specificity and efficacy. Light-based therapies offer an excellent locality and turn on/off modality to the treatment. In photothermal therapy, the nanoparticle is irradiated with a light source (LED or laser) at a specific wavelength, which is absorbed by the nanoparticle and converted into heat, causing damage to the surrounding tissue. In Photodynamic therapy (PDT), the irradiated photosensitizer, which is usually an organic molecule, generates reactive oxygen species (ROS) which cause apoptosis, DNA damage, and cell death. PDT is used in the clinic for specific cancer types, such as head-and-neck cancer.

Nanoparticles are very attractive for various applications due to their tunable physical, chemical, and biological features. Gold nanoparticles are one of the most studied due to their inert and biocompatible nature and are used in different fields such as catalysis, energy, and medicine as a theranostic agent.

In this thesis, a new type of colloidally stable gold nanoparticle with near-infrared absorbance, namely gold-gold sulfide (GGS) nanoparticles were developed. Then, these GGS nanoparticles were developed into a multifunctional nanoparticle (NP) to offer combination phototherapy; PTT and PDT for enhanced therapeutic outcome. In vitro toxicity studies of these nanoparticles and the efficacy of PTT/PDT therapy combinations of prostate cancer cell lines have been discussed.

This project is partially founded by TUBİTAK project number 119F319 and Miss. Sipahioğlu was founded by TÜBİTAK BİDEB 2210/4

ÖZETÇE

Fototerapi ve Nitrik Oksit Gaz Terapi için Altın/Altın Sülfür Nanoparçacıklarının Geliştirilmesi

Dilara Sipahioğlu

Kimya, Yüksek Lisans

5 Eylül 2023

Kanser ölüm oranı yüksek bir hastalıktır. Yüksek özgüllük ve etkinliğe sahip alternatif veya destekleyici tedavilere acil ihtiyaç vardır. Işık bazlı terapiler iyi bir lokalize tedavi sunar ve tedaviye aç/kapa yöntemi getirir. Fototermal tedavide nanoparçacık, nanoparçacık tarafından emilen ve çevredeki dokuda hasara neden olacak şekilde ısıya dönüşen belli bir dalga boyundaki ışık kayanı (LED ya da lazer) ışınlanır. Fotodinamik terapide (PDT), genellikle organik bir molekül olan ışınlanmış fotosensitizer, apoptoz, DNA hasarı ve hücre ölümüne neden olan reaktif oksijen türleri (ROS) üretir. PDT klinikte baş-boyun kanseri gibi spesifik kanser türleri için kullanılır.

Nanoparçacıklar ayarlanabilir fiziksel, kimyasal ve biyolojik özelliklerinden dolayı çeşitli uygulamalar için oldukça ilgi çekicidir. Altın nanoparçacıklar biyouyumlu karakterlerinden ötürü üzerinde en çok çalışılan parçacıklardan biridir. Bu özellikleri sayesinde teranostik ajan olarak kataliz, enerji ve tıp gibi farklı alanlarda kullanılabilmektedir.

Bu tezde, yakın kızılötesi absorbansa sahip yeni bir koloidal kararlı altın nanoparçacığı türü olan altın-altın sülfür (GGS) nanoparçacığı geliştirildi. Bu GGS nanoparçacık daha sonra kombinasyon fototerapisi sağlamak için çok işlevli bir nanoparçacık (NP) halinde geliştirildi; gelişmiş terapötik sonuç için PTT ve PDT. Bu nanoparçacıkların in vitro toksisite çalışmaları ve prostat kanseri hücre hatlarında PTT/PDT terapi kombinasyonlarının etkinliği tartışılmıştır.

Bu proje kısmi olarak TÜBİTAK proje numarası:119F319 ve Sayın Sipahioğlu TÜBİTAK BİDEB 2210/A tarafından desteklenmiştir.

ACKNOWLEDGEMENTS

First of all, I would like to express my sincere gratitude to my advisor, Prof. Havva Yağcı Acar, for the opportunities she provided. She motivated me with her support, knowledge, and patience. Being in her group and learning many things from her was an honor.

I would like to thank Prof. Uğur Ünal for his helpful scientific discussion and help with characterizations. I would like to thank Dr. Yağız Morova for his support and help with laser studies. I would sincerely like to thank Dr. Pınar Tatar for her limitless support. I would like to thank Asst. Prof. Safacan Kölemen and Prof. Burçin Ünlü for being on my thesis committee. My appreciation goes to all members of Koç University Surface Science and Technology Center (KUYTAM) for their support of characterizations.

I am deeply grateful to my dear lab partner, Mine Demir, for her limitless help and support. She was there whenever I needed her help and support. I would like to thank Gözde Demirci, who was my mentor at first and taught her knowledge about gold nanoparticles and in vitro studies. I owe special thanks to Dr. Kübra Onbaşlı, Eda Çelikbaş, Ece Çakır, Ahmet Ferid Fırat, Pelda Akın, and Kübra Özvural for their support and friendship during my studies. My appreciation extends to all former and current Polymers and Nanomaterials Research Group members.

I am deeply grateful to my family for their endless love, support, and motivation. Without them, I could not pursue my dreams. I would like to deeply thank my significant other for his endless love, support, and encouragement. My journey would be very hard without him, and I owe him many thanks. My appreciation extends to all my friends who support me.

Finally, I would like to acknowledge the Scientific and Technological Research Council of Türkiye (TÜBİTAK, project number:119F319) for their generous support and for giving me the BIDEB 2210/A scholarship. This

Table of Contents

List of Tables

List of Figures

List of Shema

Abbreviations

3MPA	3-mercaptopropionic
Da	Dalton
DI	deionized
DLS	Dynamic Light Scattering
DMSO	Dimethyl sulfoxide
DU145	Human prostate carcinoma
EtOH	Ethanol
FBS	Fetal Bovine Serum
FTIR	Fourier Transform Infrared Spectra
GNP	Gold Nanoparticles
GGS	Gold-gold sulfide
$HAuCl_4$	Auric acid
IC_{50}	Half maximal inhibitory concentration
LDH	Lactate dehydrogenase
MTT	Thiazolyl blue tetrazolium bromide
$NaBH_4$	Sodium borohydride
Na_2S	Sodium sulfide
$Na_2S_2O_3$	Sodium thiosulfate
NIR	Near-infrared
PBS	Phosphate buffered saline
PC3	Human prostate carcinoma
PDT	Photodynamic Therapy
Pen/strep	Penicillin/streptomycin
PS	Photosensitizer
PTT	Photothermal therapy
RT	Room temperature
SD	Standard deviation
-SH	Thiol

SPR	Surface Plasmon Resonance
TEM	Transmission electron spectroscopy
TUBITAK	Scientific and Technological Research Council of Türkiye
TGA	Thermal gravimetric analysis
UV	Ultraviolet
XPS	X-ray photoelectron spectroscopy
XRD	X-ray diffraction

Chapter 1:
Introduction

1.1 Gold Nanoparticles

Colloidal gold has been in our lives since the 4th century as colored glasses used in cathedrals and churches. Modern scientific research started in the 1850s with Michael Faraday. Michael Faraday discovered ruby gold and started to study the optical properties of colloidal gold[1,2]. Due to quantum size confinement, gold nanoparticles (GNPs) differ from their bulk by unique size-dependent features. GNPs show different colors and catalytic activities than their bulk. Colloidal GNPs are colored due to the absorbed and scattered light known as the localized surface plasmon peak (LSPR) phenomenon. The color of GNPs varies from red-pink to blue-black depending on the size and shape of the nanoparticle. As the size of the gold nanoparticles increases, the color changes from pink to black[3]. Nowadays, GNPs are used in drug delivery, tumor detection, gene therapy, photothermal therapy, radiotherapy, toxic gas detection, biosensor, and catalytic activities.

1.1.1 Surface Plasmon Resonance

When gold nanoparticles are exposed to light with a larger wavelength than their size, the electrons on the conductive bands are polarized and start to oscillate coherently, known as surface plasmon resonance (SPR) (Figure 1.1)[4]. SPR is measured by absorption or scattering and is affected by the size, shape, and surroundings due to the electric field density changes. SPR can be red-shifted by increasing the nanoparticle size or by tuning the size from spherical to anisotropic (Figure 1.2)[5].

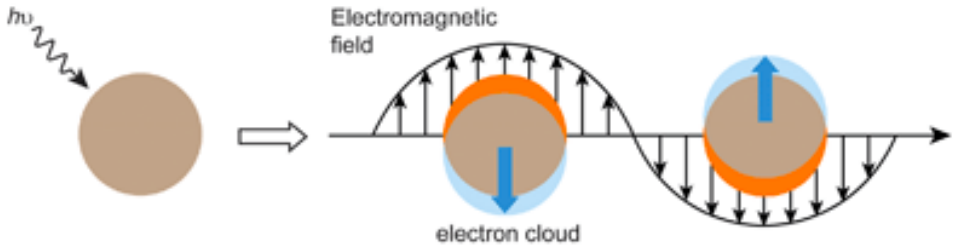

Figure 1.1: Schematic representation of SPR[4]

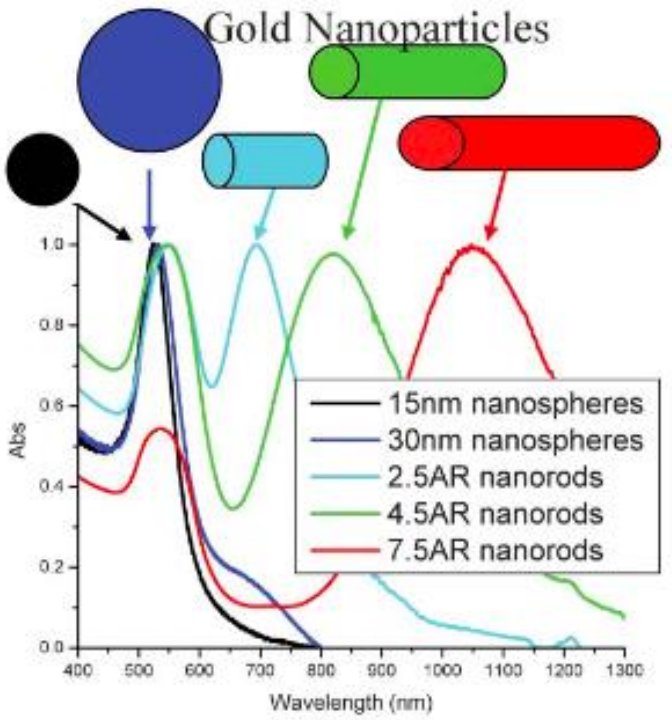

Figure 1.2: Gold nanoparticles absorption band with different size and shape[5]

1.1.2 Synthesis of Gold Nanoparticle

Gold nanoparticles are composed of two parts: inorganic core and organic coating. The absorbance of the particle is affected by the size of the inorganic core, while the organic coating is used to functionalize the surface and stabilize the particle by passivating the particle's surface. Mainly, there is two synthesis technique: top-down and bottom-up (Figure 1.3). In the top-down approach, the bulk gold is divided into small pieces until nano size is reached using molecular

beam lithography, laser ablation, reactive ion etching, or wet chemistry etching. In the bottom-up approach, nanoparticles are formed by nucleation starting from the atomic level. Generally, metallic salts are reduced by a reducing agent and capped by a stabilizing agent to prevent aggregation. There is mainly two synthesis method of Au NPs, the Turkevich and Brust-Schiffrin method.

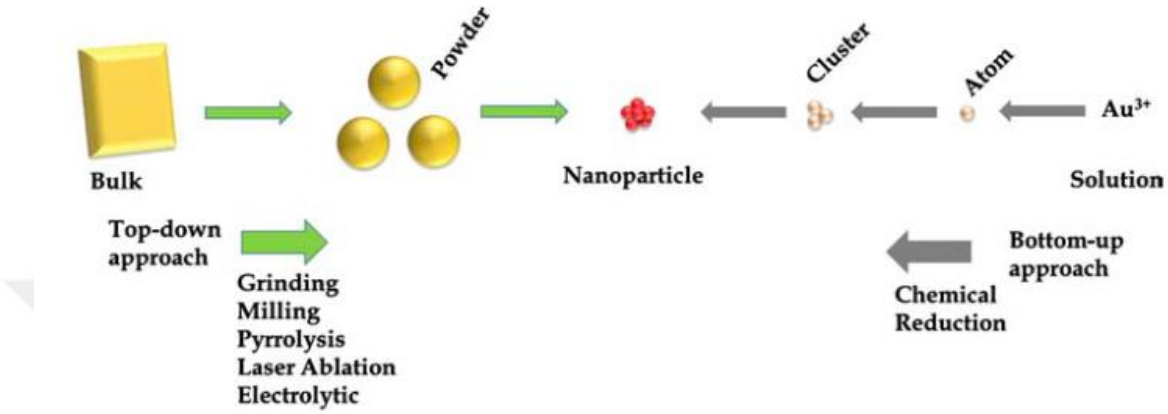

Figure 1.3: Schema of basic approach of nanoparticle synthesis [6]

In the Turkevich method, simply hot auric acid solution is reduced by sodium citrate, which is used as both a reducing and capping agent, and wine-red colloidal gold nanoparticle solution is obtained. By this method, monodispersed particles were formed with a size around 20 nm[7,8] and polydisperse nanoparticles with a larger size than 20 nm[6]. By changing the ratio of Au^{+3}/citrate, the nanoparticle size can be tuned. As the ratio of citrate increases, the particle size decreases due to excess capping agents that prevent further aggregation. Further research is done by modifying this method to control the size of particles, the seed-mediated method. In the seed-mediated method, seeds are formed by using a mild concentration of gold precursor and citrate. Then, by adding further gold precursor and citrate, more reduced gold is formed and deposed on the surface of the seeds. A precise size of gold nanoparticle solution can be obtained by controlling the ratio of seed solution and growth solution[6].

The Brust-Schiffrin method is a two-phase synthesis method. Simply auric acid is transferred to the organic phase (toluene) by tetraoctylammonium bromide (TOAB) as phase-transfer catalysis and reduced with sodium borohydride in the

presence of dodecanethiol, where dodecanethiol is the capping agent (Figure 1.4). Particles synthesized by this method are hydrophobic and have a size of up to 3 nm with dark brown color[9]. The shape of the particles is mainly cuboctahedral and icosahedral, and the particles are very stable. A year later, Brust et al. published a modified method that uses single-phase and a polar solvent like methanol. The one-phase method can be used as long as the thiol group is soluble in the same solvent as the gold precursor. As the thiol ratio increases, the particle size decreases, as with the Turkevich method. Also, smaller and monodispersed particles can be obtained by fast addition of the reducing agent and low reaction temperature.

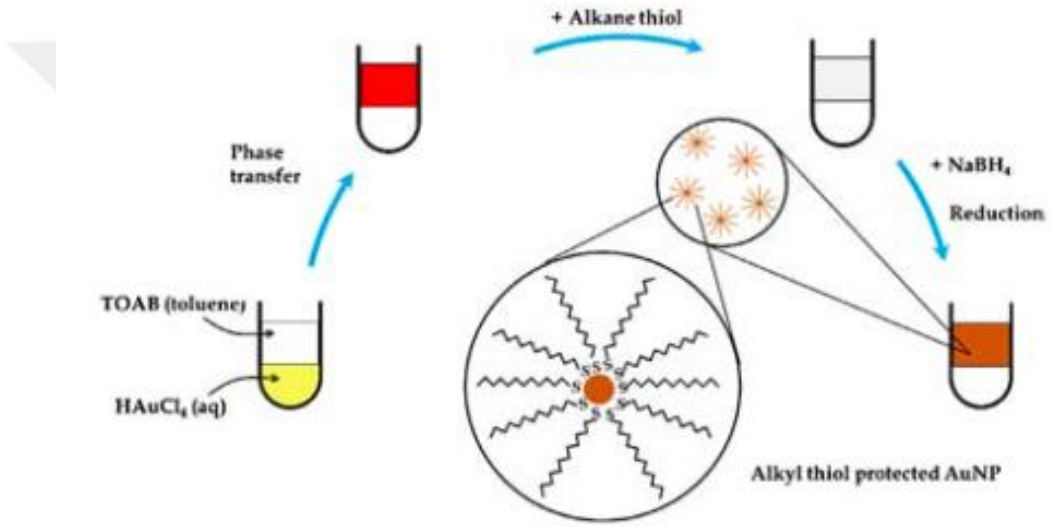

Figure 1.4: Shema of the Brust-Schiffrin synthesis method[6]

1.2 Gold-Gold Sulfide Nanoparticles

Gold nanoparticles have an absorbance peak at around 510-600 nm. Nowadays, research focuses on nanoparticles with absorbance in the near-infrared region (NIR), which has an absorbance window of 650-1500nm. NIR wavelength is more useful in medical applications because NIR light has a deeper tissue penetration (10 cm), and the absorbance by tissue and blood is at a minimum level while it is harmless[10]. Some research has been done to shift the absorbance peak of Au NPs to a longer wavelength to form aggregates by changing the pH or adding some salt[11,12]. On the other hand, NIR-absorbing Au NPs can be designed by synthesizing non-

spherical ones such as nanorods, nanostars, and nanoplates. Non-spherical Au NPs have two LSPR peaks, one at around 520 nm and the other at the NIR range[13–17]. However, these methods do not have an easy procedure, and these particles are hard to reproduce.

In 1994, Zhou et al. published an Au NP derivative with two LSPR peaks, one at 520 nm and one between 600-900, named gold-gold sulfide nanoparticle (GGS)[18].

1.2.1 Synthesis of Gold-Gold Sulfide Nanoparticle

In 1994, a two-step synthesis method of GGS was reported by Zhou et al.[18]. In the first step, auric acid ($HAuCl_4$) solution and sodium sulfide (Na_2S) were mixed at room temperature to form the unstable gold sulfide(Au_2S) particles. Then, a second portion of Na_2S was added to reduce gold on the surface of Au_2S. Finally, a mixture of 5 and 25 nm nanoparticles was obtained. In 2012, Zhang et al. reported a one-step synthesis method of GGS by reacting $HAuCl_4$ with sodium thiosulphate ($Na_2S_2O_3$)[19]. Since, Na_2S is an unstable chemical and can form variant sulfur compound during aging, which cause a lack of reproducibility. $Na_2S_2O_3$ is a final and stable form of Na_2S thus, Zhang et al. achieved synthesis are reproducible GGS by adjusting the molar ratio of $HAuCl_4/Na_2S_2O_3$. They obtained small spherical and large non-spherical particles but lack of stability.

1.2.2 Stabilization of nanoparticle

Producing colloidally stable gold nanoparticles is challenging. So far, nobody reported a colloidally stable and reproducible gold-gold sulfide nanoparticle in the literature. Stable nanoparticles are required in biological applications due to the interaction between the nanoparticle and the drug or biological media. When particles come close to each other, they form agglomerates. When the agglomerates cannot overcome the gravitation forces, they sink and form precipitations. To prevent the formation of agglomerates, nanoparticles can be stabilized by electrostatic, steric, electrosteric interactions, or electrostatic-steric (Figure 1.5)[20].

Electrostatic interaction is composed of attractive and repulsive forces between charged molecules. The same charges repel each other, so coating the nanoparticle with a small, charged molecule such as 3-mercaptopropionic acid (3-MPA) and sodium citrate. The particles will repel each other, which will prevent the formation of agglomerates. The charge of a particle can be determined by zeta potential, and a particle is accepted as colloidal unstable when the zeta potential is between -30 mV and +30 mV due to insufficient charge repulsion[21].

Stabilization can be done by steric interaction, too, by coating the particle with a neutral big molecule such as poly (ethyl glycol) (PEG) steric hindrance is obtained. Steric hindrance prevents the particles from coming close to each other, so agglomerates cannot be formed for precipitations[22–24].

Further stabilization can be achieved by electro-steric interaction, composed of both steric and electrostatic interaction. For electro-steric stabilization, charged, big molecules such as poly (acrylic acid) can be used as a coating. However, many parameters can affect electrostatic interaction, such as pH, salt addition, dielectric properties, and surrounding media[21,22]. The electrostatic-steric stabilization uses the same mechanism as electrosteric stabilization, but the stabilization is obtained by coating the nanoparticle with both uncharged big molecules and charged small molecules.

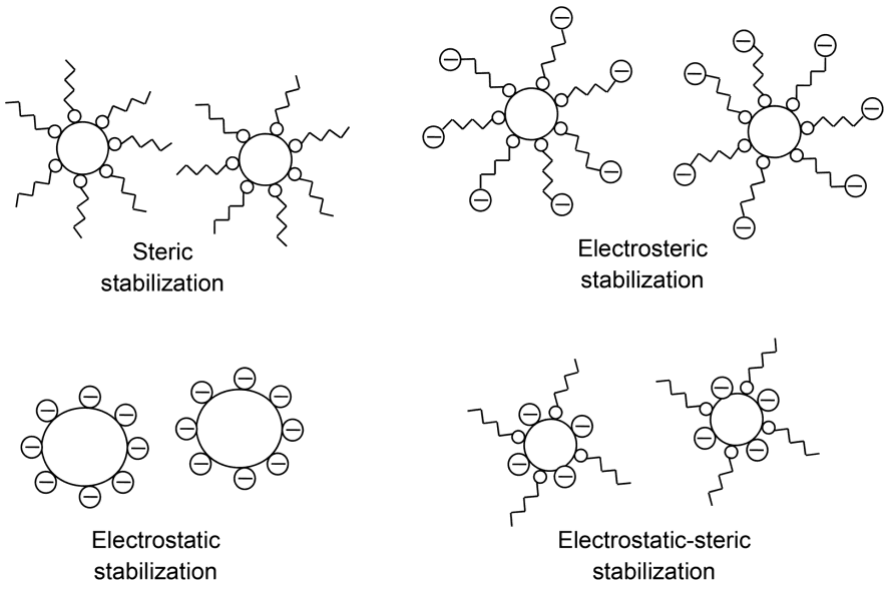

Figure 1.5: Schematic representation of nanoparticle stabilization techniques

1.3 Biomedical applications of gold and gold/gold sulfide nanoparticles

Gold nanoparticles are used mainly in biomedical applications thanks to their size and shape tunability, inert and biocompatible properties, and low toxicity. Gold nanoparticles can be functionalized by using a targeting agent and/or can be used as a drug and gene delivery system. GNPs are also known as radiosensitizers (Figure1.6)[25].

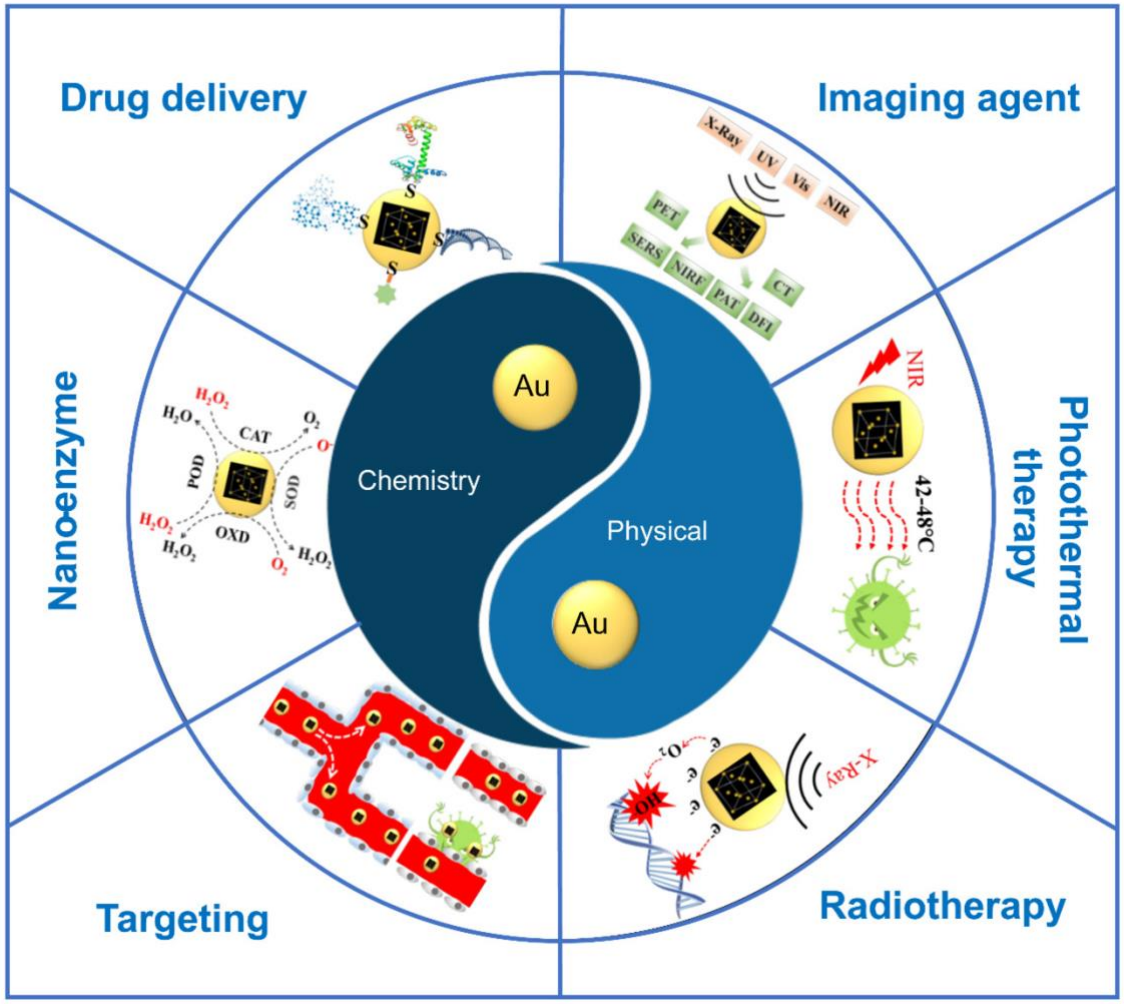

Figure 1.6: Biomedical application of gold nanoparticles[25].

1.3.1 Photothermal therapy

The number of deaths caused by cancer is over 9 million globally, so research on cancer treatment has gained high importance over the years. Classic clinical treatments such as chemotherapy, radiotherapy, and surgery have many side effects and reduce the patient's quality of life. Therefore, research on non-invasive treatment attracts high importance. Thermal therapy is a non-invasive treatment with minimal side effects. Thermal therapy can be classified basically into three categories: hyperthermia, diathermia, and thermal ablation. In hyperthermia, the cells' temperature increases by 4°C to 9°C, and this increase causes protein denaturation, which leads to cell death. Hyperthermia can be applied locally, regionally, or to the whole body. However, local hyperthermia is preferred, which damages only the tumor and protects healthy tissue. Diathermia involves a temperature increase of up to 4°C, which does not lead to cell death, but the cells become more sensitive to radiofrequency or drugs. Thus, diathermia is used with other therapy, such as radiotherapy and chemotherapy.

Different techniques can be used for thermal therapy: radiofrequency ablation, microwave ablation, and photothermal ablation. In radiofrequency ablation, the temperature of the tissue near the probe is increased by the applied radiofrequency. In microwave ablation, instead of radiofrequency, electromagnetic waves are used. The electrons of water molecules in the exposed area are aligned with the direction of applied electromagnetic waves, which cause an increase in energy that leads to a temperature increase.

In photothermal therapy, the light absorbed by a photothermal agent is converted to heat, which causes more localized hyperthermia that further protects the healthy tissue. Preferentially, NIR (700-1000 nm) light is used due to the transparency of the biological tissue and greater penetration depth of the light. Nanoparticles are extensively used in this technique due to their unique optical and magnetic properties. Basically, when the nanoparticle absorbs the light, the electrons in the conductive bands excite and gain kinetic energy during nonradiative relaxation to return to the ground state. This kinetic energy causes a temperature increase in the nanoparticle. Then, the nanoparticle transfers this heat to the

surrounding tissue, which causes hyperthermia. The gold nanoparticles have gained interest as photothermal agents due to their inert, biocompatible, and nontoxic properties. Furthermore, gold nanoparticles with complex structures have a higher heating efficiency due to the higher light absorption by elongated and sharp-end structures.

In vitro study of photothermal therapy (Figure 1.7) involves the transfection of nanoparticles into the cells and incubation at 37°C for a certain period. Then, the cells were irradiated with the laser, which causes hyperthermia and induces cell death. The temperature increase strongly correlates with the number of internalized nanoparticles by the cells. The internalization number of nanoparticles can be tuned by incubation time, size, shape, and surface functionalization[26].

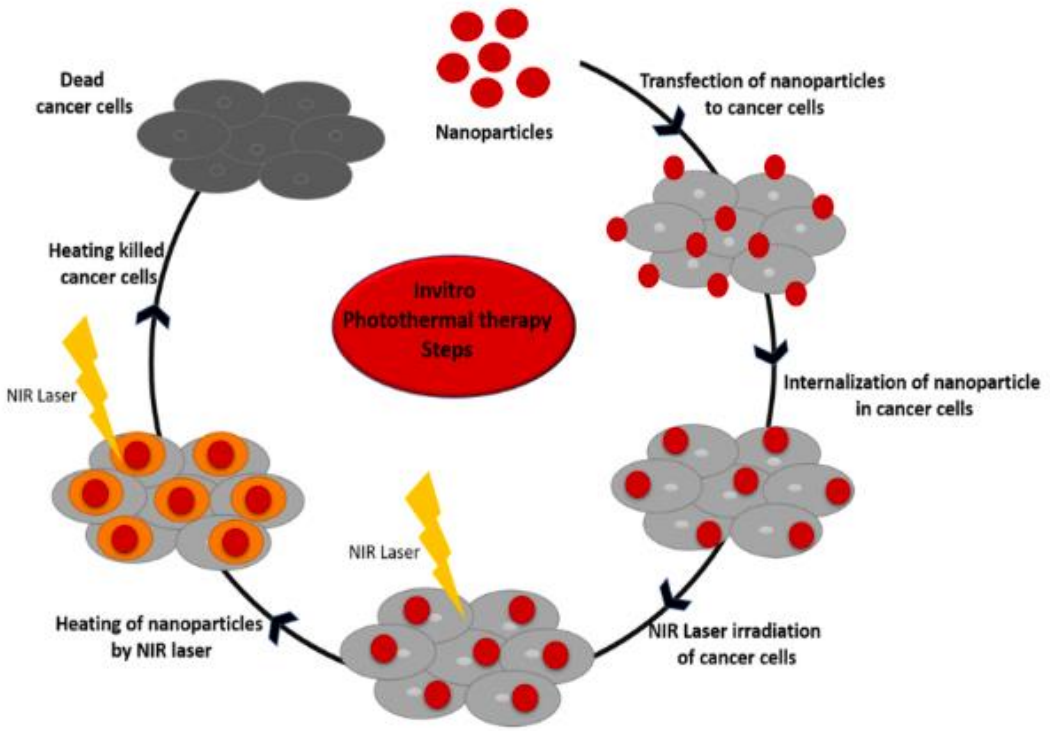

Figure 1.7: Schematic representation of in vitro photothermal therapy study steps[26]

1.3.2 Photodynamic therapy

In the mid-20th century, the clinical usage of photodynamic therapy started to be used among other cancer therapies. Photodynamic therapy is a minimally invasive

therapy that is nontoxic for healthy tissue while causing tumor cell death. Photodynamic therapy uses a nontoxic drug or dye known as photosensitizer (PS). After the internalization of the photosensitizer by cancer cells, the cells are irradiated with a specific wavelength of light. Subsequently, to laser irradiation, photosensitizers generate reactive oxygen species (ROS) in the presence of oxygen. Reactive oxygen species comprise hydroxyl radicals, singlet oxygen, and superoxide. When PS absorbs light, it is excited to a singlet PS state that can undergo intersystem crossing to form a triplet PS state. Triplet PS can undergo two different pathways to release this extra energy. Pathway 1 involves the reaction of triplet PS with substrates such as cell membrane lipids and the transfer of protons or electrons, which can form anionic or cationic organic radicals. This radical can further react with oxygen to form ROS, such as superoxide anion, hydroperoxide radical, peroxides, and hydroxyl radicals. Pathway 2 involves the reaction of triplet PS directly with oxygen molecules to generate singlet oxygen[27,28]. These two pathways can occur simultaneously, and their ratio depends on PS photochemical and photophysical features as well as the substrate and cellular oxygen concentrations. (Figure 1.8)[28].

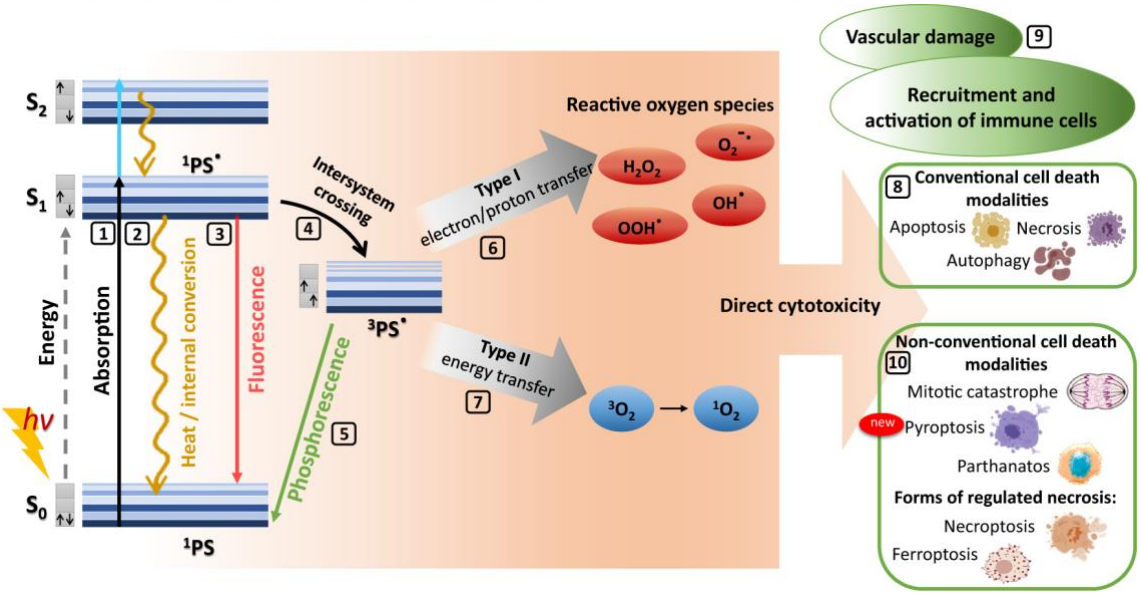

Figure 1.8: Schematic representation of photodynamic reaction[28]

To achieve the optimal PDT protocol, the tumor sensitivity to PDT should be determined first. Then, a chemical and photochemical constant PS should

accumulate selectively on the tumor side to induce photoinduced cell death. The PS and light dose concentration should be determined to obtain minimal toxicity on healthy tissue. Finally, PDT should trigger both activation of non-immunogenic and immunogenic cell death pathways to obtain distant metastatic cell death and long-lasting immunological memory to eliminate metastasis (Figure 1.9)[28]. Nanotechnology has gained interest in PDT over recent years. Nanoparticles can target tumors that accumulate PS and increase the solubility of hydrophobic photosensitizers [29].

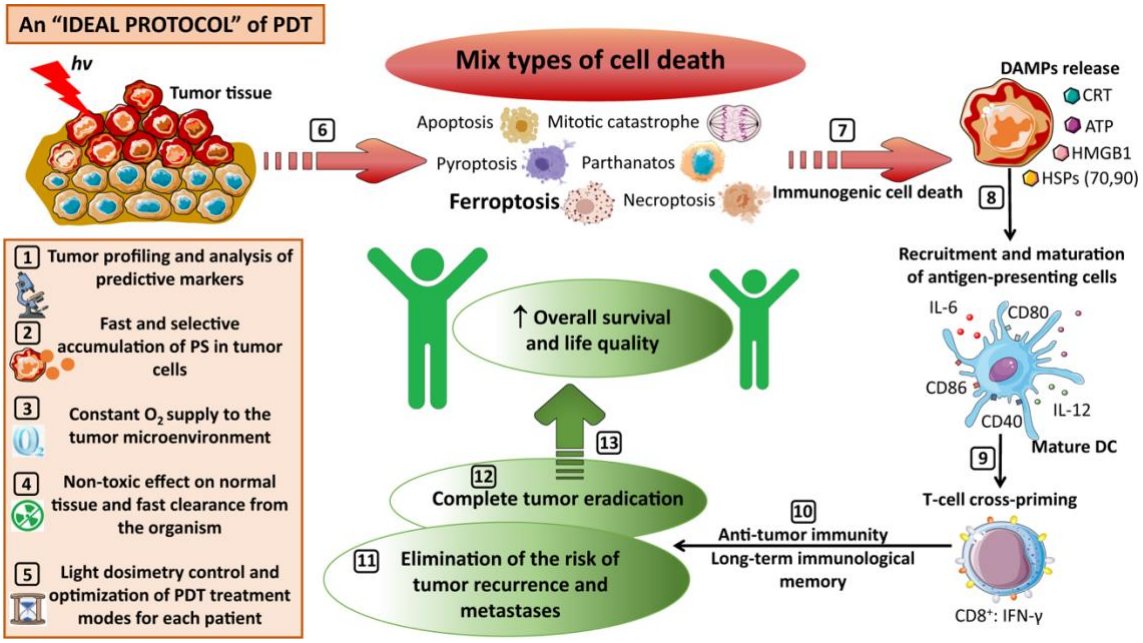

Figure 1.9: An optimal protocol of photodynamic therapy

1.4 Proposal and the aim of the thesis

The first goal of this thesis is to synthesize colloidally stable gold-gold sulfide (GGS) nanoparticles. GGS nanoparticles are preferred over gold nanoparticles because they display LSPR peak in the NIR optical window. NIR optical window is clinically preferred due to tissue transparency and greater penetration depth of light. The second goal of this project is to utilize the NIR absorbance of GGS nanoparticles to generate PTT as a localized cancer treatment method. The last goal is to load these GGS nanoparticles with photosensitizers to achieve localized

phototherapy combination, namely PDT+PTT+NO for enhanced therapeutic effect without damaging healthy tissue.

To achieve these goals, GGS nanoparticles were synthesized in water from Au and S precursors in the presence of a thiolated acid, 3-mercaptopropionic acid (3MPA), to assure surface passivation and functionalization, which in turn should help stabilization. Then, stability was improved with electrostatic binding of L-Arginine, a NO prodrug, to GGS-3MPA. The surface of GGS nanoparticles is negatively charged due to the 3-MPA coating, while L-Arginine is a positively charged molecule, which allows the successful electrostatic loading of L-Arginine to GGS nanoparticles. L-Arginine produces NO gas when heat is applied and/or in the presence of ROS. The hypothesis here is the local temperature increase with irradiation of GGS NPs at NIR, and subsequent NO release which is toxic. Further, zwitterionic ALA is electrostatically loaded to L-Arginine loaded GGS (L-GGS) producing ALA loaded L-GGS which will be called as AL-GGS. Cancer cells transform ALA to PpIX, a photosensitizer, and by irradiation at appropriate wavelength (405 or 630 nm), ROS are produced. So, irradiation of these NPs may produce GGS-based PTT, ALA-based PDT and L-Arginine based NO gas therapy due to an increase in local temperature in PTT and/or ROS produced by ALA-PDT. Lastly, ALA targets PEPT1/PEPT2 transporters, hence this proposed composition may offer receptor specificity and targeted combination photo/NO therapy of cancer. The hypothesis was tested in vitro using prostate cancer cell lines. For prospective work, the PTT experiment will be repeated with a longer irradiation time to overcome HSP27 and HSP70. Also, the NO gas therapy and radiotherapy efficiency of GGS nanoparticles will be investigated.

Chapter 2:
Development of gold/gold sulfide nanoparticles

2.1 Introduction

The first scientific research on colloidal gold (ruby gold) was done by Michael Faraday in the 1850s [1,2]. Gold nanoparticle exhibits size-dependent properties distinctly from their bulk due to the quantum size confinement. Gold nanoparticles are widely used in catalytic activity, biosensors, and biomedical applications. Nowadays, biomedical research mainly focuses on nanoparticles with NIR absorbance due to deeper penetration depth and lower autofluorescence. GNPs have a characteristic absorption peak at around 550-600nm; thus, different methods are used to red-shift the absorbance band of GNPs. Research showed that pH change and salt addition form aggregate, which red-shifts the absorption peak; however, the redispersion is hard, limiting the usage[11,12]. Also, non-spherical GNPs exhibit NIR absorbance; however, they lack reproducibility and stability [13–17]. On the other hand, small-sized GGS NPs have both the characteristics of 550-600nm absorbance and 700-1200nm NIR absorbance, which make these nanoparticles excellent candidates for biomedical applications.

A two-step synthesis method was proposed by Zhou et al.[18]. First, $HAuCl_4$ was reduced with Na_2S to form unstable Au_2S. Then, a second portion of Na_2S was added to the reaction to reduce Au on the surface of Au_2S for stabilization. Finally, a mixture of 5 and 25 nm nanoparticles was obtained. However, Na_2S is an unstable chemical that complicates reproducibility. Then, a single-step synthesis was proposed with the reduction of $HAuCl_4$ with $Na_2S_2O_3$[19]. Highly reproducible small spherical and large non-spherical particle was obtained. However, these particles are unstable and aggregate over time. Surface coatings passivate the surface, which can control the crystal growth. The particle can be stabilized using charged or long-chain molecules with electrostatic, steric, or a combination of these interactions. The

coating material influences the optical properties, cytotoxicity as well as cellular uptake.

Plasmonic nanoparticles such as GNPs and GGS can transform absorbed light into heat with various fast photo-physical processes. First, subsequently of light absorption, the electron in the conductive band generates heat by electron-electron and electron-photon relaxation. Then, this heat is released to the surroundings by phonon-phonon relaxation[30]. Thus, GGS is a promising nanoparticle for photothermal therapy because of its high light-to-heat conversion efficiency and NR absorbance property.

In this work, we synthesize GGS and electrostatically load L-Arginine (L-Arg) as both therapeutic and stabilizing agents. Then, ALA was loaded for targeting and photodynamic therapy. Their structure was investigated by TEM, XPS, XRD, and FTIR. Finally, the light-to-heat conversion efficiency of this particle was investigated.

2.2 Materials and Method

2.2.1 Materials

Gold (III) chloride trihydrate ($HAuCl_4 \cdot 3H_2O$) and sodium thiosulfate anhydrate ($Na_2S_2O_3$) were obtained from Sigma–Aldrich. 3-Mercaptopropionic acid (3-MPA) and L-Arginine was purchased by Merck. 5-aminolevulinic acid (ALA) was purchased from RPI, Corp. (USA). Ultracentrifuge tubes with polysulfone filtration membranes (10 kDa) were from Sartorius (Germany). All chemicals were of the highest purity or analytical grade, and only ultra-pure water was used (18.2 MΩ, Rephile Bioscience, and Technology, Shanghai, China).

2.2.2 Instruments

The UV-Vis absorption spectrum was obtained using the Shimadzu UV-VIS-NIR spectrophotometer in the 300-1300 nm range regarding water by using 10mm long quartz cuvettes. Hydrodynamic size and zeta potentials were measured by Malvern

Zetasizer Nano ZS. Surface analysis of GGS was analyzed by Thermo K-Alpha X-Ray Photoelectron Spectrometer. XRD analysis was performed by using Bruker D8 Advanced X-Ray Diffractometer. By using the Thermo Scientific iS10 FT-IR instrument, the functional group analysis was performed between 650-4000 cm^{-1} wavenumber range with a resolution of 4 cm^{-1} with air background. TEM analysis was performed to confirm the particle sizes and shapes using Hitachi 7800 TEM. Laser-induced solution heating was performed with 800 nm continuous-wave Ti^{+3}: Sapphire laser and 640 nm continuous-wave fiber-couple diode laser. The temperature increase was measured with a k-type thermocouple.

2.2.3 Synthesis of gold-gold sulfide nanoparticles

According to the literature, the core of GGS was synthesized[31]. 8.55×10^{-3}mmol of $HAuCl_4 \cdot 3H_2O$ was mixed with 6.6×10^{-3}mmol $Na_2S_2O_3$ under vigorous stirring (500 rpm) at room temperature. After 10 min 8.55×10^{-2}mmol of 3-MPA was added as a capping agent. The reaction was stopped by the end of 30 min and washed immediately with DI water using a 10kDa ultracentrifuge tube to get rid of excess reagent and stored in the dark at 4°C.

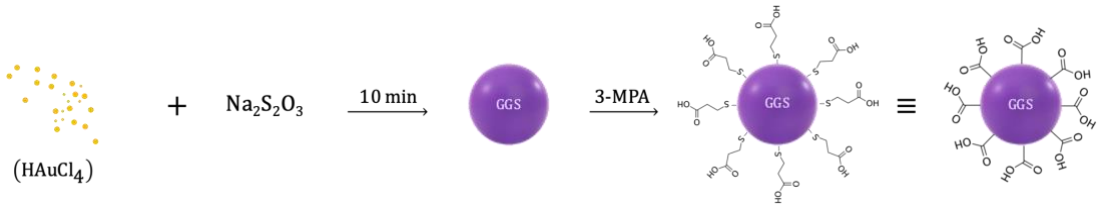

Shema 2.1: Synthesis of GGS

2.2.4 Electrostatic loading of L-Arginine onto GGS

An isothermal titration calorimetry analysis was performed to determine the complete binding of L-Arginine onto GGS. 1 ml aliquots of 0.3 mg/ml GGS in water was titrated with 5 mg/ml L-Arginine (240ul) with a rate of 5ul/s (10min of equilibration time was set between each injection). During the experiment, the temperature was stable at 25°C. According to the isothermal titration calorimetry results, a maximum of 0.83 mg of L-Arg is loaded onto 1 mg GGS. Accordingly, L-Arg

was slowly added into the GGS solution and stirred in the stirrer for 2 hours at 400 rpm at room temperature.

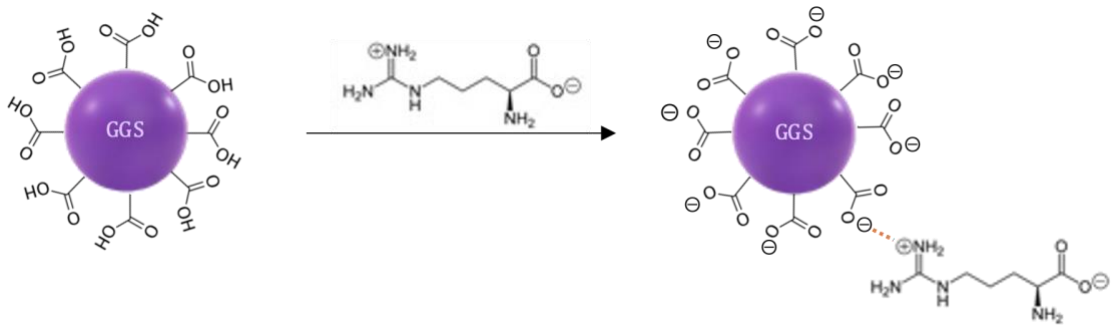

Shema 2.2: Synthesis of L-GGS

2.2.5 Electrostatic loading of 5-aminovulenuic acid onto L-GGS

1 ml aliquots of 0.34 mg/ml GGS in water was titrated with 5 mg/ml ALA (240ul) with a rate of 5ul/s (10min of equilibration time was set between each injection). During the experiment, the temperature was stable at 25°C. According to the isothermal titration calorimetry results, a maximum of 0.21 mg of ALA is loaded onto 1 mg L-GGS. Accordingly, ALA was slowly added into the L-GGS solution and stirred in the stirrer for 3 hours at 400 rpm at room temperature.

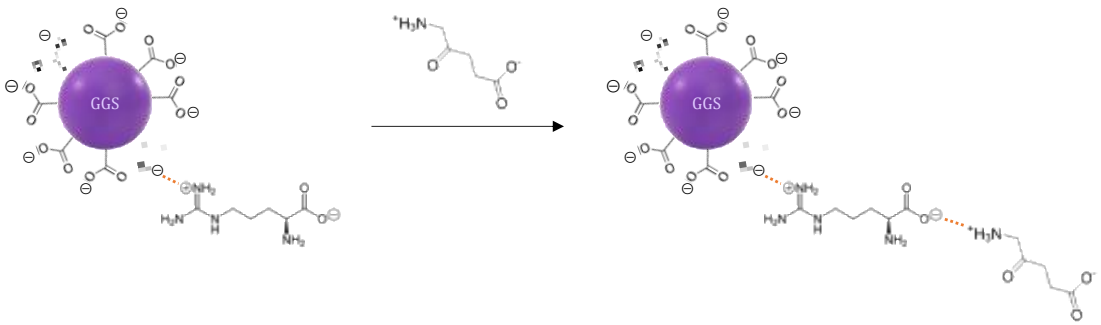

Shema 2.3: Synthesis of AL-GGS

2.2.6 Inorganic content of gold-gold sulfide nanoparticles

To determine the organic content of the GGS, thermal gravimetric analysis (TGA) was performed using TA Q500. Freeze-dried GGS nanoparticles were heated up to 900℃ from room temperature with a 10℃/min constant increase under a nitrogen atmosphere. 15-minute isothermal step at 100℃ was added to remove the absorbed humidity from the sample.

2.2.7 Laser induced solution heating

The temperature increase of 100 μg[Au]/ml L-GGS and AL-GGS was determined by irradiating with 640nm and 808nm laser for 30min in a polystyrene cuvette. The temperature increase was measured with a thermocouple. The stability of photothermal heating was demonstrated by three on/off cycles.

2.3 Results and Discussion

2.3.1 Synthesis and characterization of GGS

Colloidally stable GGS nanoparticles were synthesized from auric acid in a method modified from Zhang et al.[19]. Initially, $HAuCl_4 \cdot 3H_2O$ was reduced with $Na_2S_2O_3$ and 10 min after 3-MPA was added as the capping agent. This allows nucleation and growth of the crystals. The mol ratio of Au:S:3-MPA is optimized at 1:0.77:10. Colloidal GGS NPs have two absorbance peaks, one at 540nm and a broad one between 750-1300 nm and a shoulder between these two peaks (Figure 2.2a). The anionic GGS NPs has a strong surface charge (zeta potential is -28 eV) critical for electrostatic stabilization and bimodal hydrodynamic size distribution, 3.3/98.1 nm (number/intensity-based average) (Table 2.1). The organic content of GGS is 23.3% (Figure 2.2b).

Next, L-Arg was electrostatically loaded to these anionic GGS NPs producing L-GGS (L-Arg loaded GGS NPs). The pKa values of the carboxylic acid, primary amine, and guanidine groups are 2.2, 9.0, and 12.5, respectively. GGS NPs have an anionic

surface due to carboxylate groups; thus, the NH_3^+ group of L-Arg electrostatically bind to the GGS surface. Upon electrostatic loading, the shoulder between 540nm and 750-1300nm disappears, and the intensity of the NIR peak increases significantly. Also, the hydrodynamic size changed from 3.3/98.1 to 2/69-3 (number/intensity-based average) and the zeta potential changed from -28 eV to -45 eV (Table 2.1). These may indicate the disassembly of the loose aggregates (Figure 2.2a). Indeed, 3MPA coated GGS NPs were prone to some agglomeration upon centrifugation, however, when L-Arg was loaded colloidal stability over a year was observed.

For photodynamic therapy, 5-aminolevulinic acid (ALA) was electrostatically loaded as a protoporphyrin prodrug to the L-GGS. The pKa values of carboxylic acid and primary amine of ALA are 4.05 and 8.9, respectively. At its zwitterionic state ALA binds from its NH_3^+ group electrostatically to the anionic L-GGS NPs. After electrostatic loading, the UV-Vis spectra and hydrodynamic size did not change significantly. Hydrodynamic size changed from 2/69-3 to 1.8/65-4 (number/intensity-based average). The zeta potential changed from -45 eV to -42.4 eV (Table 2.1).

Electrostatic loading of L-Arg and ALA onto GGS was first tested and confirmed via titration of GGS NPs the agents using nano-isothermal titration calorimetry (nano-ITC). According to Figure 2.1, as 3-MPA coated GGS NPs were titrated with L-Arg and then L-GGS NPs were titrated with ALA exothermic enthalpy changes and a saturation point were observed, which proves the electrostatic loading (Figure 2.1). The dissociation constant (K_d) for L-Arg and ALA was 9.85×10^{-5} and 5×10^{-8}M, respectively which is in the acceptable range of $1\times10^{-4}M>K_d>1\times10^{-9}M$[32]. The number of peaks until the saturation point shows the maximum amount of L-Arg and ALA that can be loaded to NPs. According to the ITC results, a maximum of 0.83 mg of L-Arg can be loaded onto 1 mg GGS, while a maximum of 0.21 mg of ALA can be loaded onto 1 mg L-GGS. This formulation was used for the rest of the studies reported in this thesis.

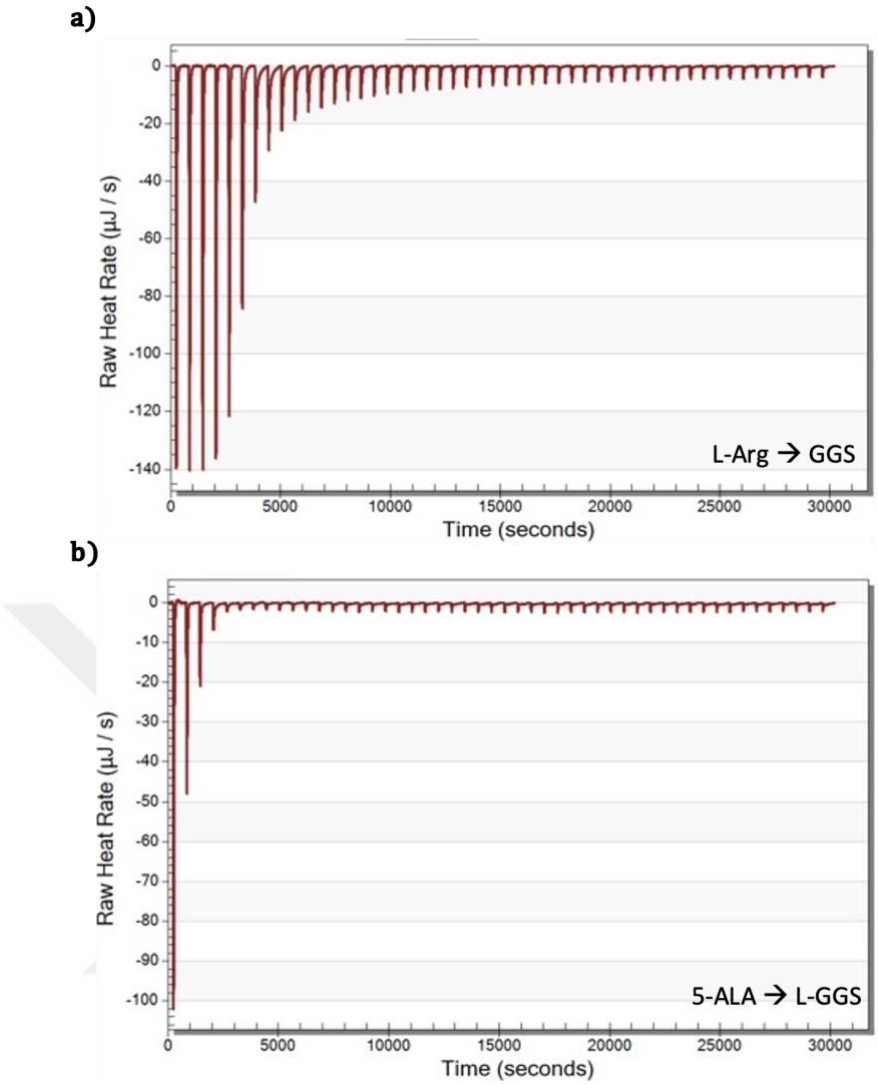

Figure 2.1: Nano-ITC results of L-Arg and ALA loading on GGS and L-GGS respectively

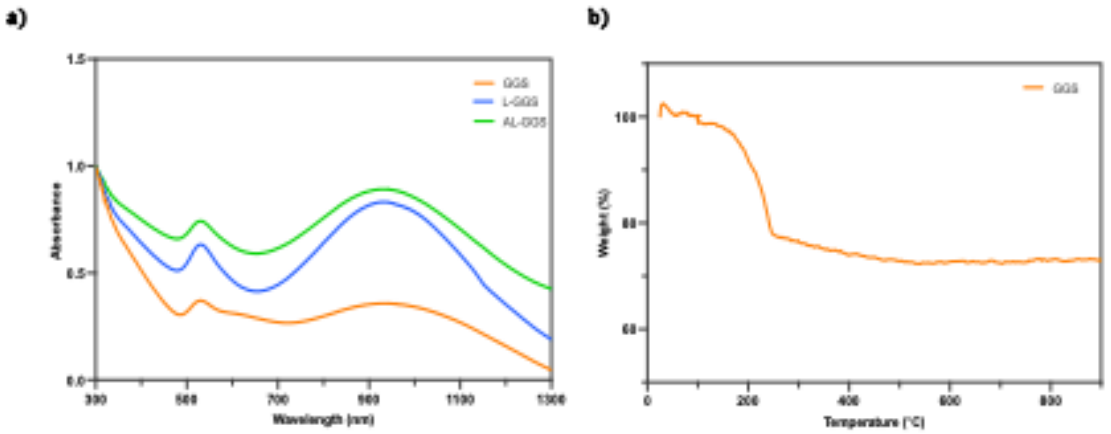

Figure 2.2: a) Normalized absorbance spectra of GGS, L-GGS, AL-GGS in water. b) TGA analysis of GGS. c) FTIR spectra of GGS, L-GGS, and AL-GGS

Table 2.1: Hydrodynamic size and zeta potential of GGS in water

Sample	Dh-number [a] (nm)	Dh-intensity [b] (nm)	Zeta potential (mV)
GGS	3.3	98.1	-28
L-GGS	2	69-3	-45
AL-GGS	1.8	65-4	-42.4

Error! Unknown switch argument. *Hydrodynamic size reported by DLS was reported as the number average.*

Error! Unknown switch argument. *Hydrodynamic size measured by DLS was reported as the intensity average.*

According to the FT-IR spectra of GGS, we did not observe a stretching band between 2550-2600 $cm^{-1,}$ which confirms that the thiol group of 3-MPA is bound on the surface of gold. The strong stretching band at 1708 cm^{-1} was assigned to the C=O stretching from the carboxylic acid. For L-GGS, the broad band between 2500-3500 cm^{-1} is assigned to the stretching of O-H of the carboxylic group. The stretching band of the guanidino group was observed in both L-GGS and L-Arg at 1625 cm^{-1} and 1635 $cm^{-1,}$ respectively. Also, amide II stretching bands at 1543 cm^{-1} and 1558 cm^{-1} was observed for L-GGS and L-Arg, respectively. Finally, the C-N stretching for the amine group was observed at 1171 cm^{-1} and 1177 cm^{-1} for L-GGS and L-Arg, respectively. The guanidino, amide II, and C-N stretching indicates the successful loading of L-Arg to GGS. The band at 1640 cm^{-1} corresponds to the C-N stretching of the imine group. The C=O stretching of the ketone group was observed at 1738 cm-1 and 1732 $cm^{-1,}$ corresponding to AL-GGS and ALA, respectively. The C=O stretching of AL-GGS is observed to be very small due to the high signal intensity of the N-H bending of the amine group. The C=O stretching approved the successful loading of ALA to L-GGS (Figure 2.3).

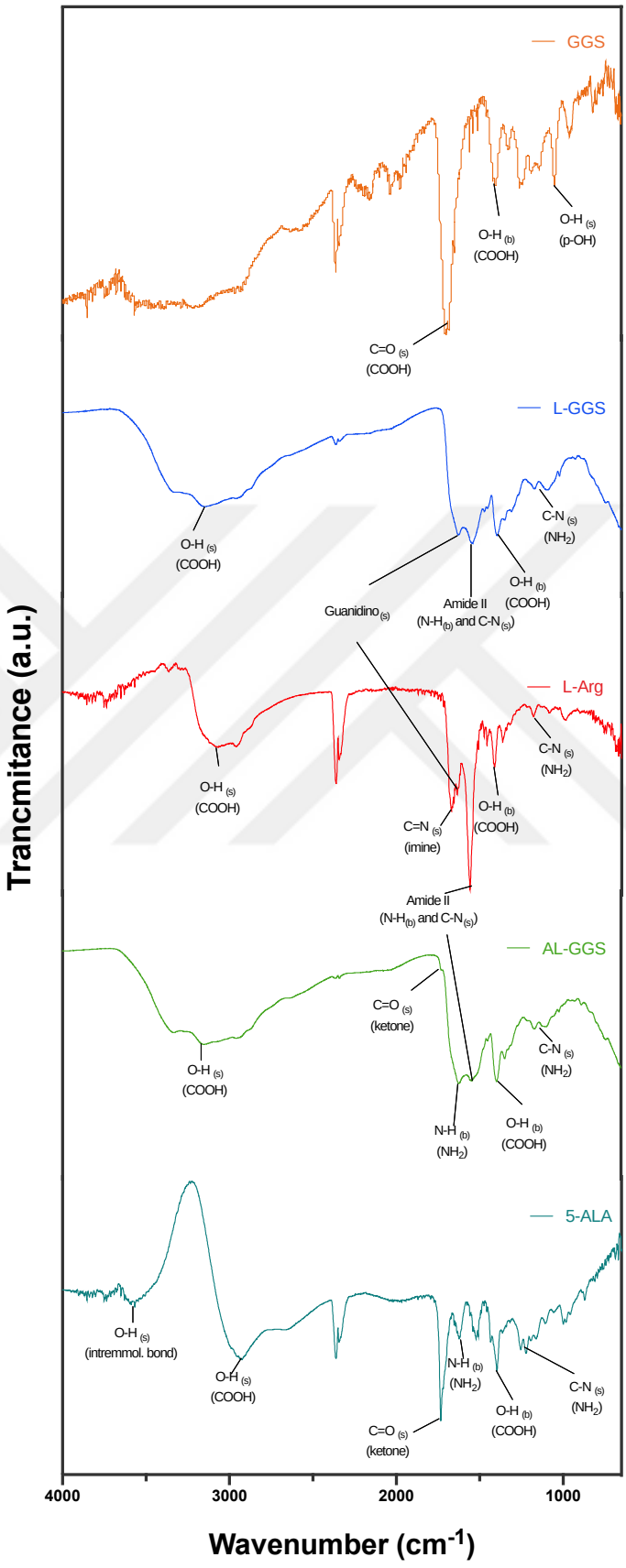

Figure 2.3: FTIR spectra of GGS, L-GGS, AL-GGS, L-Arg, and ALA

GGS has 2θ values of 32.6, 36.6, 38.5, 44.7, 52.0, 64.9, and 78.5 that correspond to the $Au_2S(111)$, $Au_2S(200)$, Au(111), Au(200), $Au_2S(220)$, Au(220), and Au(311) diffraction peaks, respectively (Figure 2.4a). The Au_2S and Au peaks are assigned according to PDF-04-007-4652 and PDF-00-066-0091. Since the crystal size is very small, the $Au_2S(111)$ and $Au_2S(200)$ are broad and thus overlap and are observed as one broad peak. Au peaks showed a face-centered cubic (fcc) crystal system with a 225-space group, while Au_2S showed a simple cubic crystal system with a 224-space group (Figure 2.4a). %-Crystallinity was calculated as 42.7%. The crystal size of the gold nanoparticle calculated with the Au(111) peak was found as 6.73 nm, while the crystal size of the gold sulfide nanoparticle calculated with $Au_2S(111)$ and $Au_2S(200)$ was found as 3.19 nm. The ratio of GNP:GGS was 13:1 using Topas software fundamental method Rietveld. Indeed, the exact structure of the GGS NPs are not clear in the literature and not clear here, either.

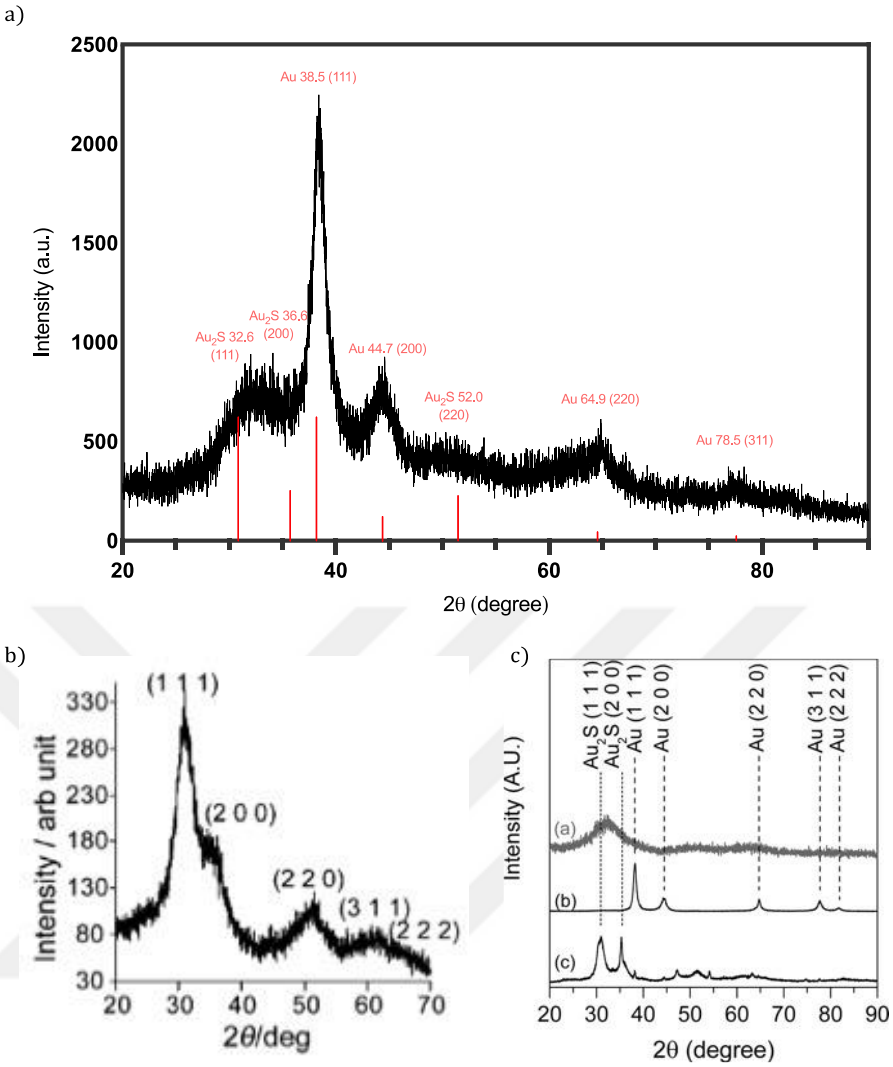

Figure 2.4: Figure 2.4: a) XRD spectra of GGS. b) XRD spectra of Au2S-incorporated ferritin[33]. c) XRD of Au2S (c) (Sigma-Aldrich)[34]

XPS analysis showed one type gold and one type sulfur peaks at 83.86 eV of Au $4f_{7/2}$ corresponding to metallic gold (Au^0), and 162.34 eV of S $2p_{3/2}$ of Au-S bond which is due to Au-3MPA binding (Figure 2.5). However, the binding energy of Au^+ was not observed coming from the Au-S bond. According to the literature, the small peak separation and the domination of the Au^0 peak prevent the observation of Au^+ binding energy[35]. Depth profile analysis of 20-layer etch was performed to determine the structure of GGS. Before etching, the ratio of Au:S was 1.27:1, while after 20 layers of etching, the ratio of Au increased to 7.35:1. The outer layer of GGS is composed of coating, which has S that confirms the higher S ratio. However, since the material is not a thin film, depth analysis does not necessarily indicate inner atoms. Depth analysis did not show any other type of S either.

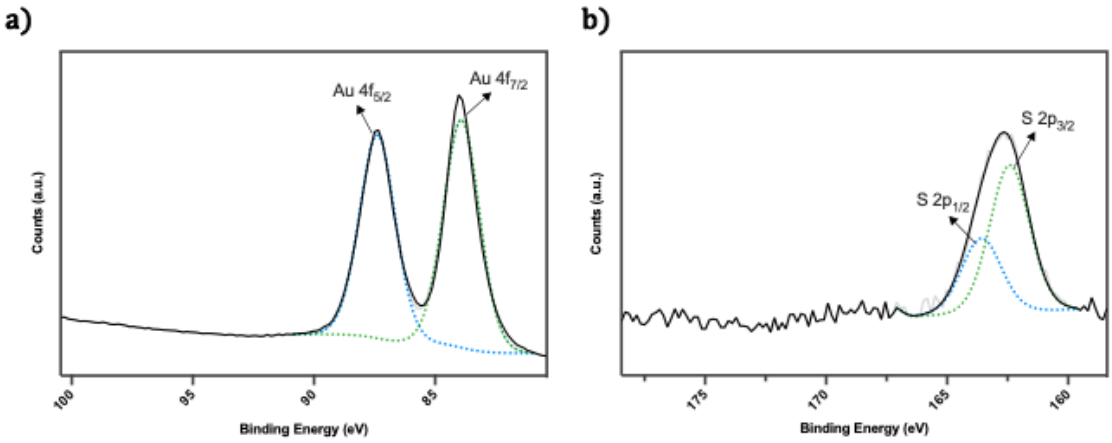

Figure 2.5: a) Au 4f and b) S 2p XPS spectra of GGS

According to the TEM images, GGS consists of small-spherical and larger non-spherical particles that agrees well with the two SPR peaks. Non-spherical particles consist of rods, triangles, truncated triangles, and hexagons (Figure 2.6). The d-spacing of the deltoid and the rod was found as 2.7 Å. The diameter of the small-spherical particles is around 3 nm while the diameter of small anisotropic particles are around 12 nm, and the edge of rods are around 20 nm. On the other hand, the edge of larger anisotropic particles range between 20-45 nm. The size of small-spherical and large non-spherical is in correlation with DLS measurement.

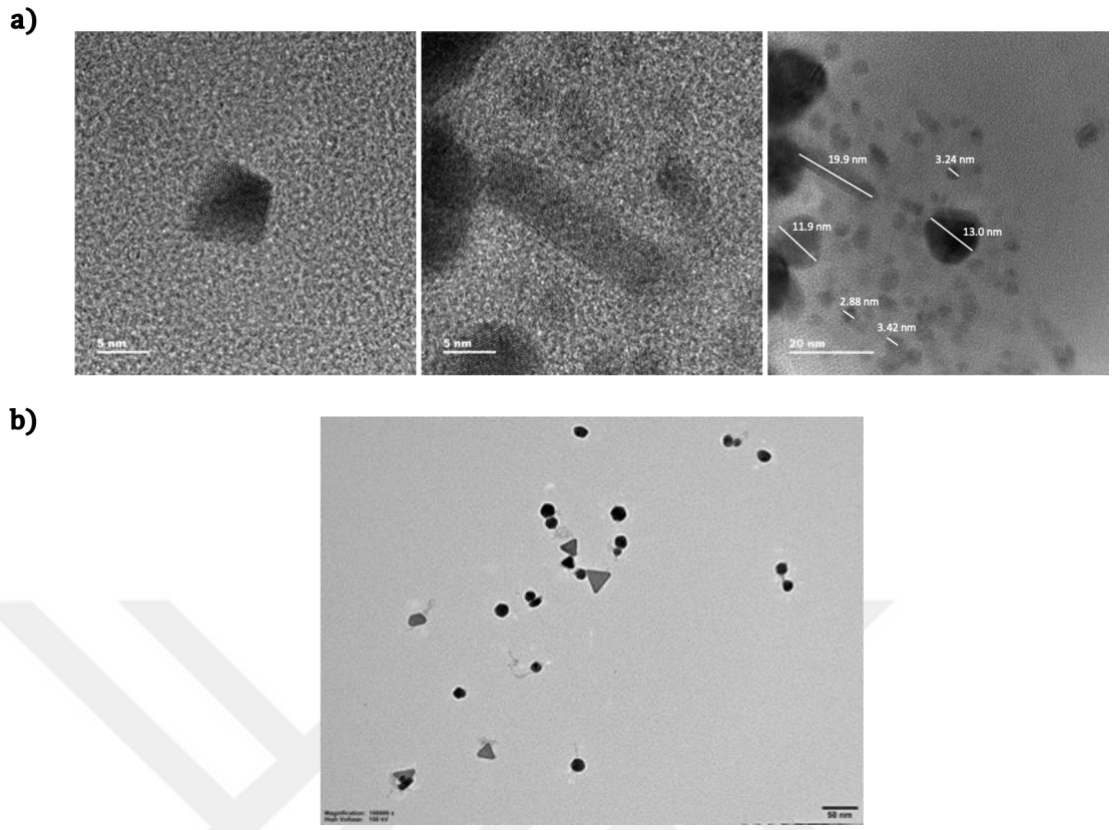

Figure 2.6: a) High resolution TEM image b) TEM image of GGS

2.3.2 Properties of GGS NPs

Light-to-heat conversion of GGS NPs is critical for PTT. This was tested at visible and NIR wavelengths. Despite the NIR peak maximum of GGS NPs are between 900-950 nm, the laser that is available for our studies is at 808 and 795 nm, so we have worked with 640 nm and the NIR lasers. Irradiation of aqueous L-GGS (100 µg [Au]/mL) with 640nm and 808nm laser for 20 min caused an average of 9°C and 10.5°C temperature increase, respectively. AL-GGS showed an average of 10.1°C and 11.8°C temperature increase after 20 min irradiation with 640nm and 808nm laser, respectively (Figure 2.7a and 2.7b). Light-to-heat conversion efficiency was 55.1% and 63% for L-GGS irradiated with 640nm and 808nm laser, respectively. On the other hand, the light-to-heat conversion efficiency of AL-GGS was 67.6% and 58.6% after irradiation with 640nm and 808nm laser, respectively. Both L-GGS and AL-GGS showed a stable light-to-heat conversion after three on/off laser irradiation cycles (Figure 2.7c).

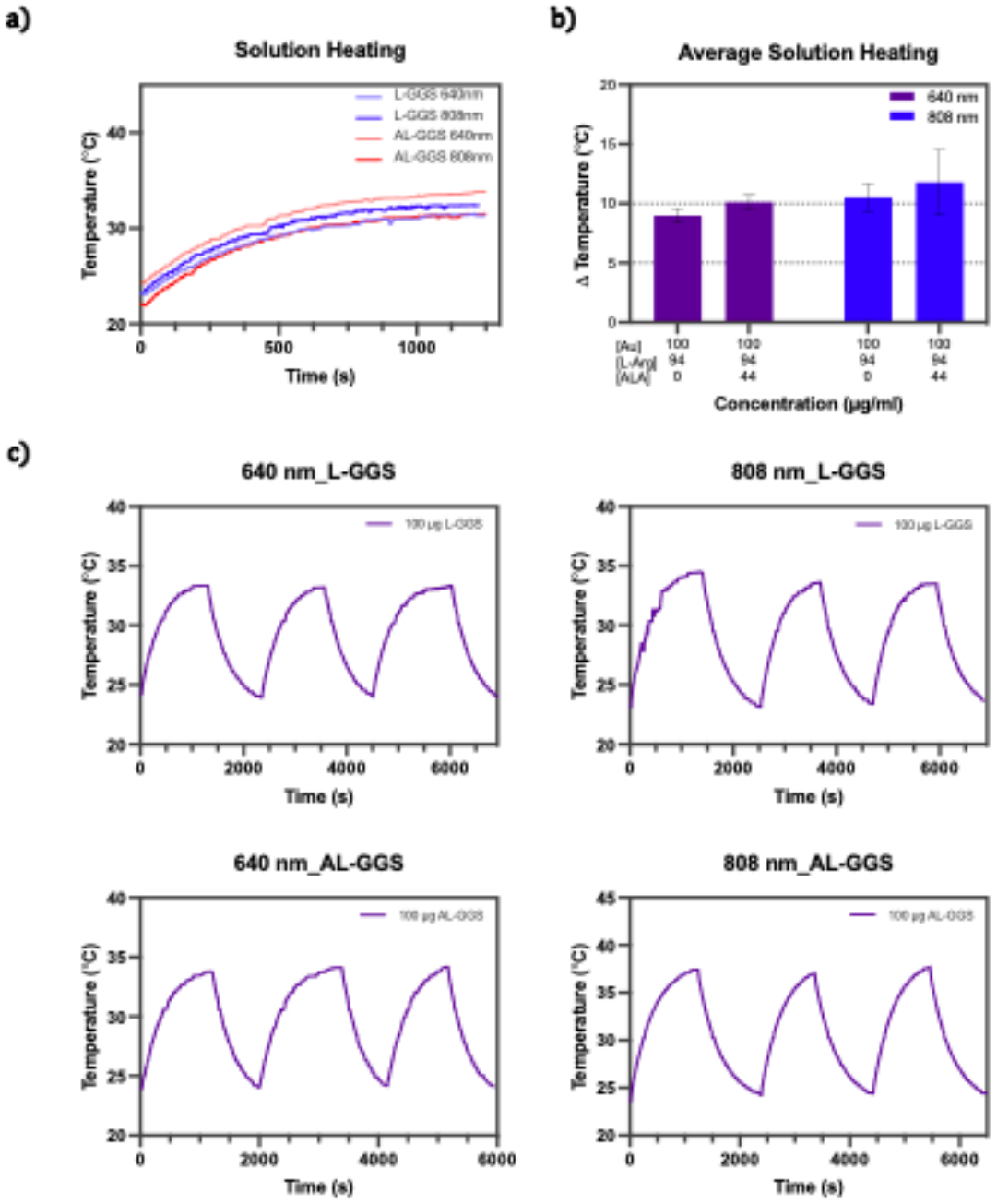

Figure 2.7: a) Solution heating b) Average solution heating c) on/off solution heating stability of L-GGS, AL-GGS with 640 and 808 nm laser

2.4 Conclusion

In this study, aqueous anionic GGS NPs were synthesized in a single simple step with visible and NIR SPR bands (540nm and 750-1300nm) successfully. The size distribution of GGS comprises both small spherical particles and bigger anisotropic

particles with different shapes, such as rods and triangles. L-Arg as NO producer and ALA as a PDT prodrug were sequentially loaded to the GGS NPs successfully utilizing electrostatic interaction of the NP surface with the agents. This provided colloidally stable therapeutic GGS NPs. All GGS solutions showed a significant temperature increase with laser irradiation.

Chapter 3:
Gold/gold sulfide nanoparticles for photothermal and photodynamic therapy

3.1 Introduction

Phototherapies have attracted attention over the years due to the minimally invasive and localized procedure. Photothermal therapy consists of light absorption by a thermal agent converted to heat. Among nanoparticles, gold nanoparticles attract attention due to their inert and biocompatible properties. NIR light is preferred in photothermal therapy due to biological transparency and higher penetration depth. Thus, gold/gold sulfide nanoparticle with NIR absorbance is highly promising in photothermal therapy.

In photodynamic therapy, ROS formation is generated by exciting photosensitizer with light. PS are classified as first, second, and third generation. First-generation PS consists of a hematoporphyrin derivative. The second generation consists of porphyrins, bacteriochlorins, phthalocyanines, etc. On the other hand, third-generation PS consists of the conjugation of PS to nanoparticles as nanocarrier. Nanoparticle-based PS can target tumors and can increase the solubility of hydrophobic PS[36,37].

5-aminolevulinic acid (ALA) is a prodrug of protoporphyrin IX (PpIX), widely used PS in PDT. ALA is an endogenously produced amino acid in mitochondria. In the heme synthesis pathway, ALA is converted to PpIX. Exogenous addition of ALA to the tumor side causes the over-accumulation of PpIX, which makes it highly suitable for PDT (Figure 3.1)[38].

In this study, we investigated the potential of L-GGS and AL-GGS as PTT and PDT agents. In vitro toxicity and PTT/PDT efficiency of these nanoparticles were investigated using PC3 and DU145 prostate cancer cell lines.

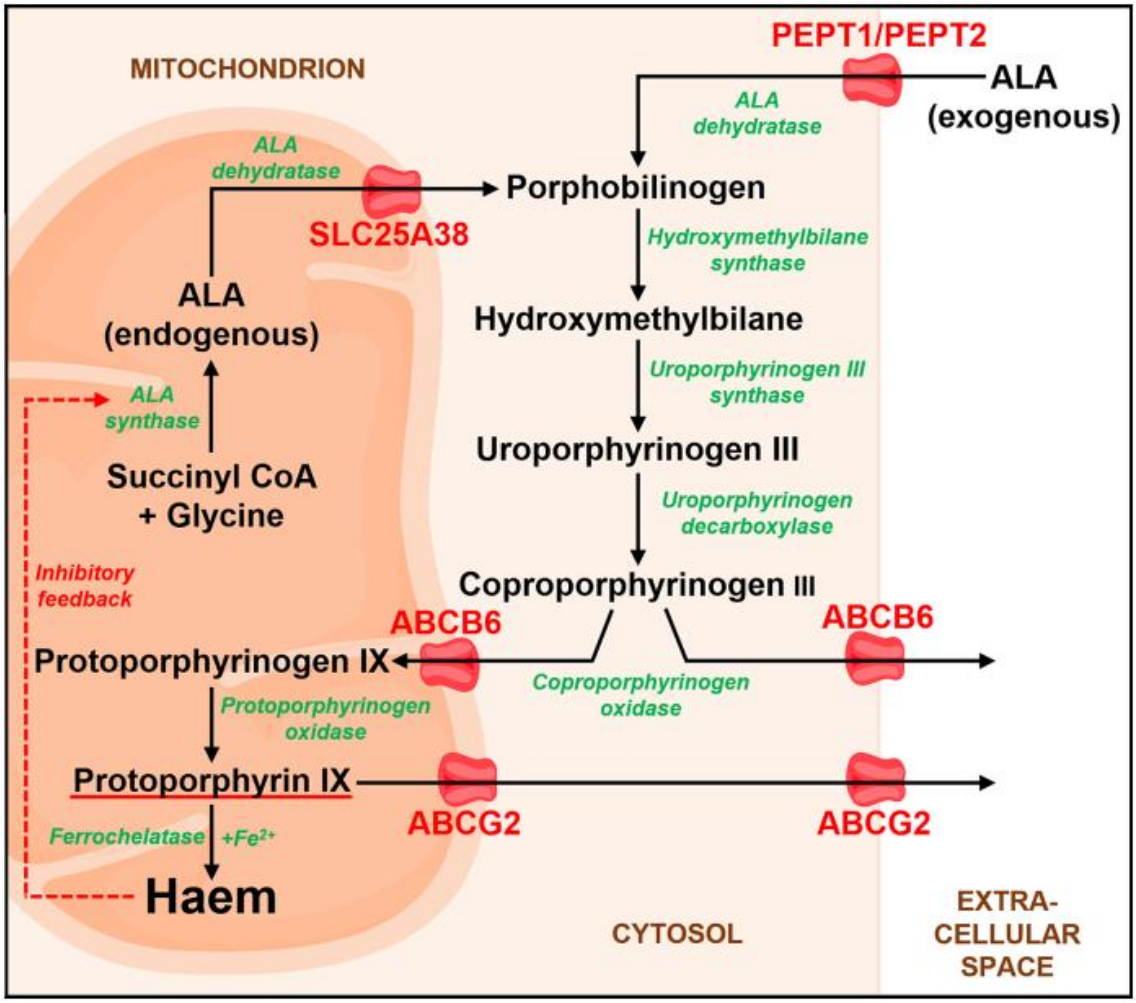

Figure 3.1: PpIX conversion by heme synthesis pathway of ALA[39]

3.2 Materials and Method

3.2.1 Materials

Roswell Park Memorial Institute 1640 (RPMI 1640), L-glutamine (L-glu), Penicillin-streptomycin (pen/strep), trypsin-EDTA (try), fetal bovine serum (FBS) was provided by Diagnovum (Germany). 3-(4,5-dimethythiazol-2-yl)-2,5-diphenyltetrazolium bromide (MTT) and phosphate-buffered saline (PBS) tablets were purchased from Bio-Matic Corp. While Dimethyl sulfoxide Hybri-MaxTM was obtained from Sigma (USA). Finally, 96-well flat bottom plates were bought from Nest Biotechnology Co. Ltd. (China). LDH assay was bought from Promega (USA). PC3 and DU145 cells was a generous gift from Gözüaçık Lab.

3.2.2 Instruments

The cell viability test was calculated using a Synergy-H1 microplate reader, BioTek Instruments Inc. (Vermont, USA). In vitro cell heating experiments were done by using a 640 nm continuous-wave fiber-couple diode laser and a 795 nm diode laser. The temperature increase was recorded with a thermal camera. Cell images were collected by using a live cell fluorescence microscope (Carl Zeiss, Oxio Observer Z1).

3.2.3 Cell Culture

PC3 and DU145 cells were cultivated in RPMI 1640 medium (supplemented with 10% FBS, 2% L-glu (2mM), 1% pen/strep) in a 37℃ incubator at 5% CO2-humidified atmosphere. Before passaging, the cells were washed with PBS and trypsinized with 0.05% try.

3.2.4 Cytotoxicity assay

MTT measures the mitochondrial activity by forming formazan with the mitochondrial enzyme of viable cells. Thus, it is widely used to measure the cytotoxicity.

First, cells were seeded with 10000 cells/well concentration in a 96-flat bottom well plate and incubated overnight. Then, the culture medium was changed, and the cells were treated with 0-100 µg [Au] /ml L-GGS, AL-GGS, L-Arg, and ALA for 24h as long incubation. To investigate the targeting effect of ALA, the same procedure was done, but the concentration increased to 100-150 µg [Au] /ml L-GGS, AL-GGS, L-Arg, and ALA and the incubation time decreased to 12h to eliminate passive uptake effect. After the incubation, the medium with GGS was removed, and 50µl of MTT (5mg/ml in PBS) and 150µl of fresh medium were added to each well and incubated for 3 h. Finally, the formed purple formazan was dissolved in 200µl DMSO:EtOH (1:1 v/v) solutions, and plates were shaken gently for 15 min. The cell viability was measured by reading the absorbance at 570nm with a reference

reading at 650nm in a microplate reader. The following equation was used to calculate the cell viability:

$$Cell\ viability\ (\%) = \left[\frac{Absorbance(treated)}{Absorbance(control)}\right] \times 100\ (n = 5)$$

3.2.5 Photothermal therapy

PC3 and DU145 cells were seeded with a 10000 cells/well concentration in a 96-well plate and incubated overnight. The cells were treated with L-GGS and AL-GGS between 37.5-50 µg [Au]/ml for 24h. Then, the medium was replaced with fresh medium. Cells were irradiated for 10 min from the bottom with 640 nm with a power of 280 mW at a constant 37°C environment. The temperature increase was tracked with a thermal camera.

For PC3 cells, the same procedure was done, but the concentration of L-GGS and AL-GGS was between 100-200 µg [Au]/ml, and the cells were co-irradiated for 10 min with 640 (0.73 W/cm^2) and 795 (2.08 W/cm^2) nm laser. Cell viability tests were performed with MTT assay.

3.2.6 Detection of PpIX formation

PC3 and DU145 cells were seeded with a concentration of 12500 cells/well in a 96-well plate and incubated overnight. The cells were treated with 50 µg [Au]/ml L-GGS, AL-GGS, L-Arg, and ALA for 24h. After incubation, the medium was removed, and PBS was added. Finally, images were collected with Live Cell Fluorescence Microscope (Carl Zeiss, Oxio Observer Z1) by using bright field and porphyrin filters (λ_{exc}:365 nm and λ_{em}:683 nm).

3.2.7 Photodynamic therapy

PC3 and DU145 cells were seeded with a 10000 cells/well concentration in a 96-well plate and incubated overnight. The cells were treated with 25-75 µg [Au]/ml L-GGS, AL-GGS, and corresponding concentrations of L-Arg and ALA for 24h. After incubation, the medium was changed to fresh medium, and cells were irradiated with 640 nm (0.73 W/cm^2) for 10 min. Laser-irradiated cells were incubated overnight. Then, cell viability was determined by using an MMT assay.

The same procedure was applied to determine the targeting effect of ALA, except that the cells were treated with 50-100 µg [Au]/ml L-GGS, AL-GGS, and corresponding concentrations of L-Arg and ALA for 12h.

3.2.8 Determination of ROS

PC3 and DU145 cells were seeded and treated with GGS as described in the PpIX determination study. Before 640 nm laser irradiation (0.73 W/cm^2) for 10 min, the medium of the cells was removed, and 200µl of PBS with 10µM DCFH-DA was added and incubated for 40 min. Then, laser irradiation images were collected with a live cell fluorescence microscope with a bright field and DCFH filter (λ_{exc}:470 nm and λ_{em}:525 nm).

3.2.9 LDH Assay

PC3 and DU145 cells were seeded with a 10000 cells/well concentration in a 96-well plate. The cells were treated with 50 µg [Au]/ml L-GGS, AL-GGS, and corresponding concentrations of L-Arg and ALA for 24h. After the incubation time, the medium was changed to a fresh medium. Laser-irradiated cells were incubated overnight. The medium of each group was collected into Eppendorf, and the cells were trypsinized for 5 min at room temperature. The detached cells were collected and put into corresponding Eppendorf. The cells were centrifuged at 600×g for 10 minutes. 10 µl of the supernatant medium was transferred into a new 96-well plate

(3 replicas), and 100 µl of LDH solution (composed of 100 µl assay buffer and 2 µl WST substance) was added. The cells were incubated for 30 min, and the absorbance was read at 450 nm with a microreader. LDH released from the cells oxidizes lactate, which releases NADH. NADH reacts with WST, and a yellow color is observed.

3.2.10 Statistical analysis

Statistical analysis was done using 2-way ANOVA from the GraphPad Prism 9 software package (GraphPad Software, Inc., USA). All data were expressed as mean ± standard deviation (SD), and $p<0.05$ was considered statistically significant.

3.3 Results and Discussion

3.3.1 Dark toxicity of GGS

The dark toxicity of L-GGS, AL-GGS, L-Arg, and ALA was evaluated on PC3 and DU145 prostate cancer cells using an MMT assay. Since above 80% viability is accepted as non-toxic by ISO 10993-5, all agents were safe between the studied dose range. NP does were given as the Au content of the NPs and tested between 25-100 µg [Au]/ml (Figure 3.2).

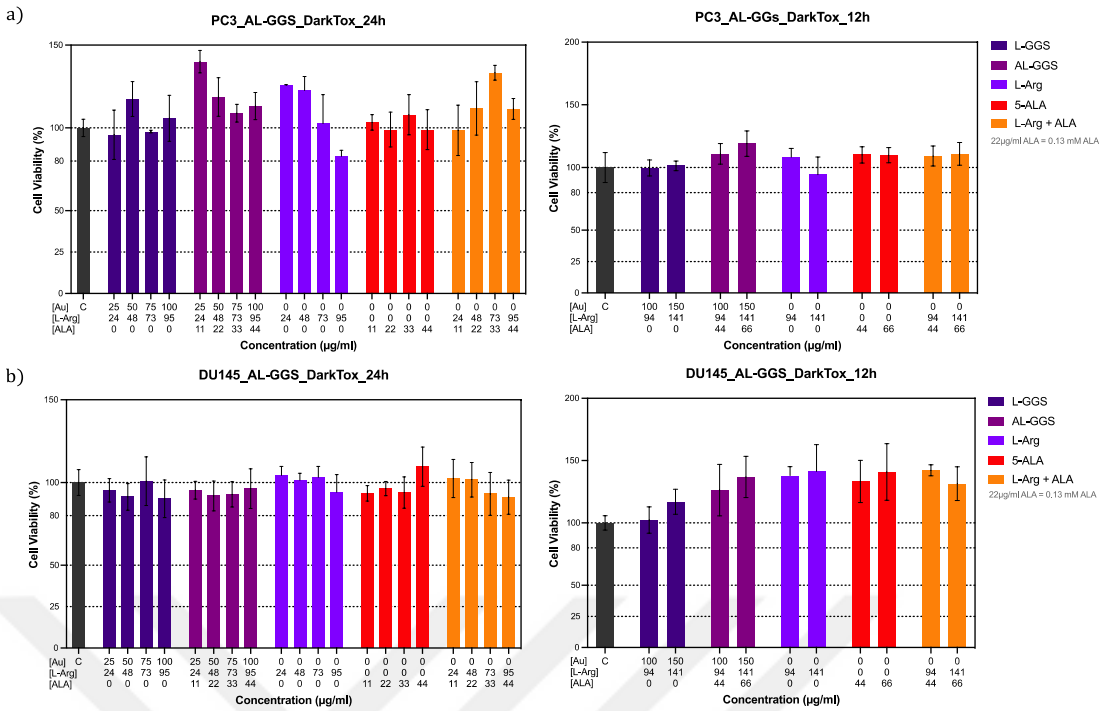

Figure 3.2: Dose-depended viability of a) PC3 and b) DU145 treated with L-GGS, AL-GGS, L-Arg, ALA after 24h and 12h incubation (n=5)

3.3.2 Determination of efficient GGS NPs and irradiation wavelength for phototherapy

Red (640 nm) laser irradiation is clinically used for ALA-PDT and as shown in Figure 2.7 triggered photothermal heating of GGS NPs. NIR 795 nm laser also triggers photothermal effect. We also have a laser system where dual wavelength irradiation is possible. In order to evaluate the effect of laser wavelength on killing cells treated with AL-GGS a set of experiments were conducted. PC3 cells treated with AL-GGS NPs between 50-200 µg [Au]/mL and irradiated separately 5 min at 640 nm, 795 nm and subjected to co-irradiation at 640 and 795 nm (Figure 3.3). For comparison PC3 cells treated with free ALA at equivalent concentration to the cargo of AL-GGS were irradiated in the same way. AL-GGS/640 nm irradiation reduced the cell viability below 25 % at the lowest dose and caused near complete loss of viability at the higher doses. However, at the high doses the cell killing was similar to free ALA and advantage of the produced particle was only clear at the lowest dose at which ALA-PDT only caused about 60% reduction in viability. On the other hand, AL-GGS/795 nm irradiation caused about 20-40% reduction in viability. Significant toxicity in ALA/795 nm protocol may arise from

two photon absorption of ALA which may also support increasing cell death when free ALA was coupled with co-irradiation. AL-GGS/co-irradiation caused dramatic losses in viability but the difference from AL-GGS/640 nm irradiation was not dramatic, suggesting ALA-PDT as the major source of phototoxicity and small contribution of GGS based PTT at 795 nm. However, the dramatic difference of ALA-PDT at 640 nm and AL-GGS/640 nm phototoxicity may originate from increased ALA internalization via NP delivery system as well as some temperature increase due to 640 nm irradiation of the GGS (Figure 2.7). Thus, only 640 nm laser irradiation was used for the rest of the studied but the irradiation time was increased to 10 min for enhanced killing.

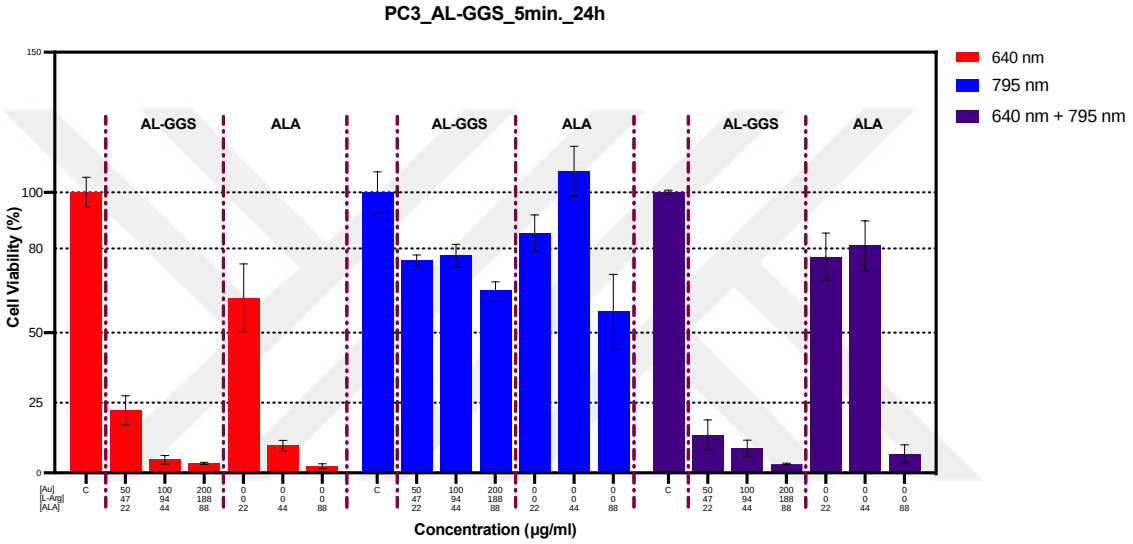

Figure 3.3: Viability of PC3 cells treated with corresponding concentration of 50-200 µg [Au]/ml AL-GGS or free ALA for 24h and irradiated with 640 nm laser (0.73 W/cm2) and/or 795 nm laser (2.07W/cm^2) for 5min

3.3.3 Photothermal therapy potential of GGS

PTT based killing triggered at 795 nm was low, hence temperature change of the irradiated cells were monitored with a thermal camera. The concentration of the particles in the cell studies were lower than the solutions used for the light-to-heat conversion studies reported in Chapter 2. At 37.5and 50 µg [Au]/ml no significant increase in temperature of the cells were observed (Figure 3.4a). Thus, a higher concentration of L-GGS (50-200 µg [Au]/ml) was tried with PC3 cells by co-irradiating with 640 and 795nm lasers for 10 min, and a temperature increase up to 9.8°C was observed at 200 ug [Au]/mL along with about 5°C increase at 50 µg [Au]/mL (Figure 3.4b). However, we could not observe a dramatic photothermal therapy effect (70% cell viability) (Figure 3.4c). The elevated heat shock protein

expression level of PC3 and DU145 can explain this[40]. For PC3 cells at 46°C 20min is required to reduce HSP70 while 12 min is enough for HSP27 to obtain IC_{50}[41]. Hence, in future studies co-irradiation for 20 min may be studied to trigger a stronger PTT effect.

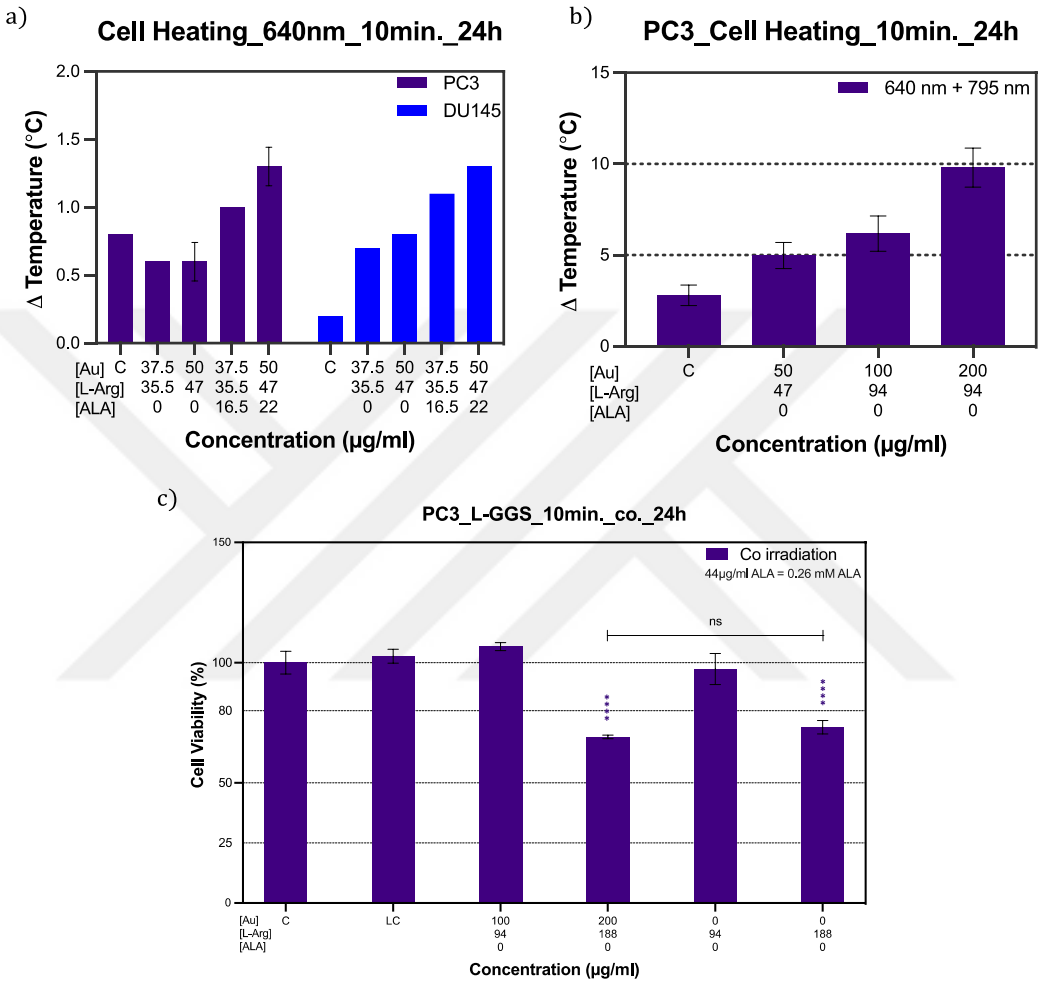

Figure 3.4: In vitro temperature increase of treated cells: a) PC3 and DU145 cells irradiated with 640 nm laser b) PC3 cells co-irradiated at 640 and 795 nm c) viability of PC3 cells after 10min 640 and 795nm co-irradiation (n=3)

3.3.4 Intracellular PpIX generation

The conversion efficiency of ALA to PpIX mainly determines the photodynamic therapy potential of ALA. ALA is a porphyrin precursor in the heme synthesis pathway, and some cancer cells convert it to PpIX more efficiently than healthy cells [38]. ALA also targets PEPT1/PEPT2 which is overexpressed in PC3 and deficient in

DU145 cells [42,43]. PC3 and DU145 cells were treated with 50 μg[Au]/ml L-GGS, AL-GGS, corresponding to 47 μg/ml L-Arg, 22 μg/ml ALA, and L-Arg+ALA for 24h. Then, the intracellular PpIX generation was determined by fluorescence microscopy (Figure 3.5). A strong PpIX red fluorescence was observed in ALA, ALA/L-Arg and AL-GGS treated cells indicating effective delivery of ALA to PC3 cells with the NP and efficient conversion to PpIX. In the fluorescence images, the PpIX accumulation in DU145 cells seems similar to PC3 cells treated with ALA. The reason is that the cell density of DU145 cells is much higher, which gives the impression of higher PpIX accumulation. For PC3, there is no significant difference in signal intensity between AL-GGS and ALA, but the signal intensity of cells co-incubated with both L-Arg and ALA is significantly lower with similar cell density. For DU145, the highest PpIX accumulation was observed in cells treated with AL-GGS, while no significant difference was observed between cells incubated with ALA and co-incubated with both L-Arg and ALA.

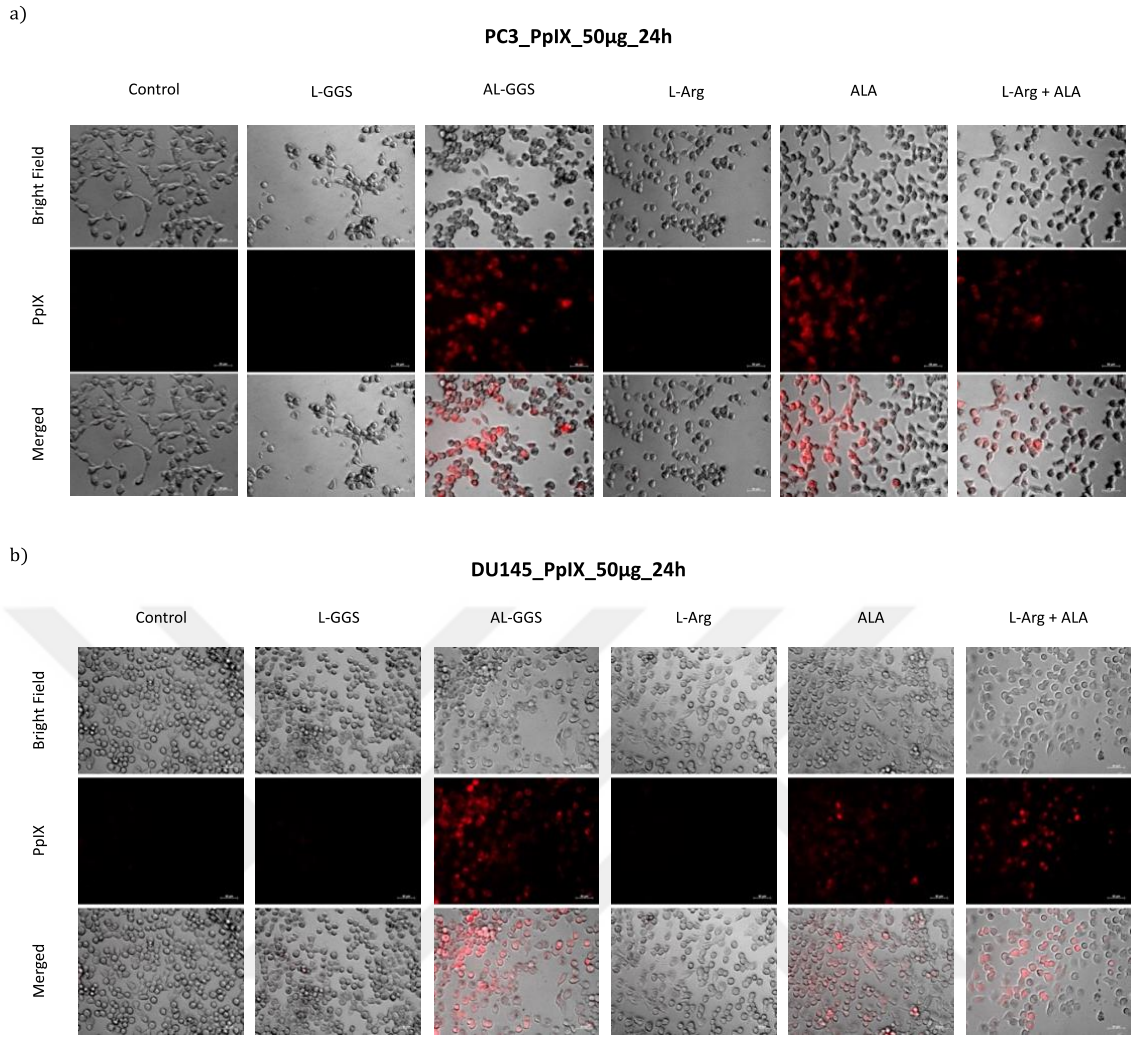

Figure 3.5: Detection of intracellular PpIX signals from the cells a) PC3 b) DU145 cells treated with 50µg [Au]/ml L-GGS, AL-GGS, L-Arg, ALA, L-Arg+ALA for 24h

3.3.5. Intracellular ROS generation

The photodynamic therapy mechanism involves the energy transfer from the excited photosensitizer to the surrounding and/or oxygen molecules to form ROS and/or singlet oxygen, respectively [44]. Thus, intracellular ROS generation is critical for successful PDT. PC3 and DU145 cells were incubated with 50 µg[Au]/ml L-GGS, AL-GGS, corresponding to 47 µg/ml L-Arg, 22 µg/ml ALA, and L-Arg+ALA for 24 h. Then cells were incubated with DCFH-DA for 40 min and irradiated with 640nm laser (0.73 W/cm^2) for 10min. Fluorescence microscopy images of the treated cells indicated a higher basal ROS level for PC3 than DU145 cells (Figure 3.6), which is in correlation with the literature[45]. In PC3 cells, there is no significant difference in

signal intensity between AL-GGS and ALA compared to DU145 cells. The highest signal intensity in PC3 cells was observed in cells treated with AL-GGS and ALA; however, no significant difference is observed between them. On the other hand, DU145 cells treated with AL-GGS showed a remarkably higher signal intensity. These findings are in correlation with the MTT assay performed in photodynamic studies, except for DU145 which is probably more resistant to ROS

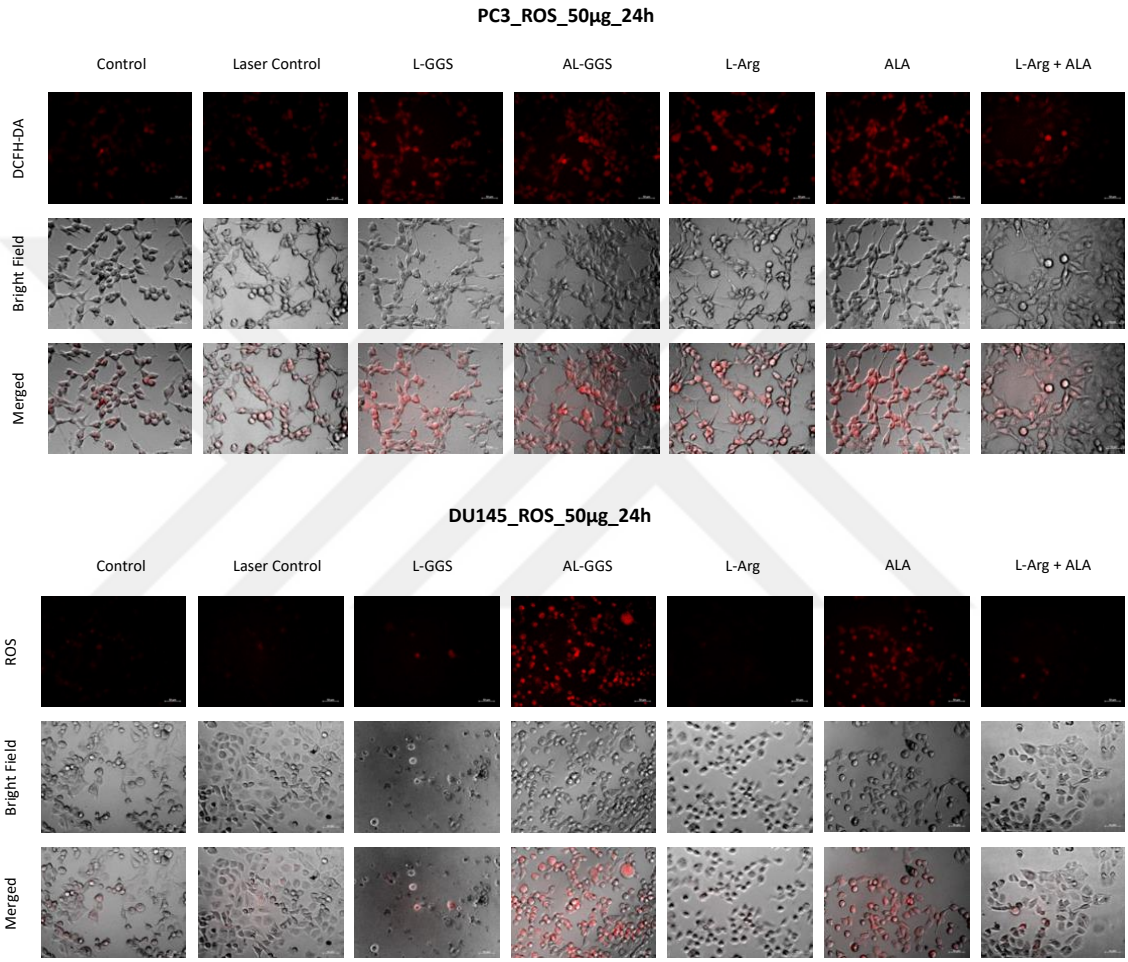

Figure 3.6: Fluorescence image of ROS generation of a) PC3 b) DU145 cells treated with 50 µg[Au]/ml L-GGS, AL-GGS, L-Arg, ALA, L-Arg+ALA for 24h

3.3.6 Photodynamic therapy

Phototoxicity of AL-GGS/640 nm irradiation protocol was further investigated in PC3 and DU145 cells. Cells were incubated between 25-75 µg [Au]/ml L-GGS and AL-GGS corresponding to 23.5-70.5 µg/ml L-Arg and 11-33 µg/ml ALA for 24h. Then, cells were irradiated with a 640 nm laser (0.73 W/cm^2) for 10 min (Figure

3.7). Laser control showed no phototoxicity, proving it as a safe laser dose. No phototoxicity was observed with cells treated with L-GGS, demonstrating that in the absence of ALA, GGS did not show phototoxicity. Free L-Arg, ALA, and co-incubated L-Arg and ALA did not show any phototoxicity except the highest dose of ALA in PC3 cells, which decreased cell viability to 70%. Since ALA targets PC3, we observed higher phototoxicity of AL-GGS in PC3 than in DU145 cells, as expected. In PC3 cells, 50 μg[Au]/ml AL-GGS decrease cell viability to 3% while 75 μg [Au]/ml cause complete cell death; however, this difference is not statistically significant. On the other hand, AL-GGS cause up to 70% reduction in viability of DU145 cells with the highest AL-GGS concentration (Figure 3.7a).

To demonstrate the targeting effect of ALA, the incubation time was decreased to 12 h to minimize the passive internalization of nanoparticles. At lower incubation time, no phototoxicity was observed at the same concentrations. Thus, the concentration was increased to 100 μg[Au]/ml GGS, corresponding to 94 μg/ml L-Arg and 44 μg/ml ALA. At this concentration, the cell viability of PC3 decreased to 40%, while the cell viability of DU145 was decreased by only 30%. This difference successfully demonstrates the targeting effect of ALA on PC3 cells (PEPT1/PEPT2 channels (Figure 3.7b).

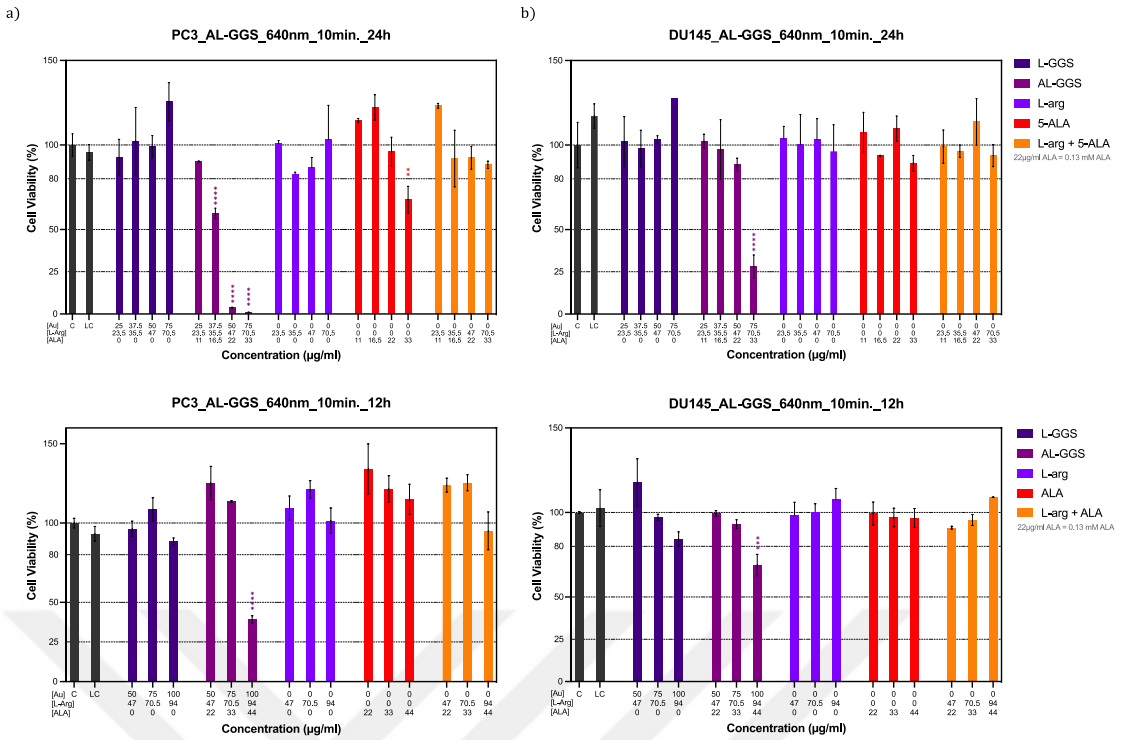

Figure 3.7: Viability of a) PC3 and b) DU145 cells, treated with corresponding concentrations of 25-75 µg [Au]/ml L-GGS, AL-GGS, L-Arg, ALA, L-Arg+ALA for 24h and 12h incubation and irradiated with 640 nm laser (0.73 W/cm²) for 10min

3.3.7 LDH assay

Lactate dehydrogenase is an enzyme quickly released to cell culture media after loss of cell membrane integrity. For DU145 cells with no laser treatment, the LDH levels were the same. However, DU145 cells treated with AL-GGS and laser showed a significant increase in LDH release. On the other hand, PC3 showed a higher basal LDH release. LDH released by cells treated with AL-GGS and laser was significantly higher in PC3, and a significant difference was observed with DU145 cells (Figure 3.7).

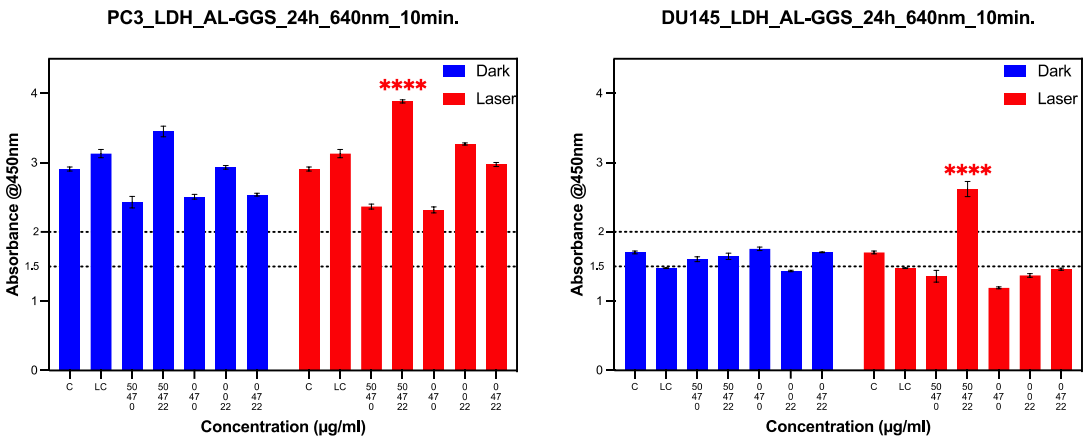

Figure 3.8: LDH assay of a) PC3 and b) DU145 treated with NPs and 640 nm laser

3.4 Conclusion

This study showed the cytotoxicity, photothermal, and photodynamic therapy potential of L-GGS and AL-GGS NPs. Photothermal therapy efficiency was low due to the high expression of HSP in PC3 and DU145 cells. In contrast, highly efficient photodynamic therapy, may be coupled with mild hyperthermia and possible with ROS triggered NO release from L-Arg, was obtained with AL-GGS at 10 min 640 nm irradiation. The cell viability drops to 3% even though the concentration of ALA was low (0.13mM). The targeting effect of ALA was observed with high expression of PEPT1/PEPT2 in PC3. These findings indicate that GGS can be a good nano-transporter of ALA.

Chapter 4:

Perspectives for future studies

In this work, GGS was designed and structurally analyzed to investigate the potential application in cancer therapy. L-Arg was electrostatically loaded to increase the colloidal stability, and ALA was loaded as a targeting agent and PpIX prodrug. The PTT potential can be investigated by prolonging the laser irradiation time. L-Arg is a NO prodrug; thus, the contribution of NO gas therapy should be examined further. Gold nanoparticles are used as a radiosensitizer. Thus, the radiotherapy potential of GGS is also under investigation.

Sipahioğlu, D., Demir, M., Sennaroğlu, A., & Yağcı Acar, H. Development of gold/gold sulfide nanoparticles for phototherapy. (In preparation)

Bibliography

(1) Reddy, V. Gold Nanoparticles: Synthesis and Applications. *Synlett* **2006**, *2006* (11), 1791–1792. https://doi.org/10.1055/s-2006-944219.

(2) Faraday, M. X. The Bakerian Lecture. —Experimental Relations of Gold (and Other Metals) to Light. *Philosophical Transactions Royal Soc Lond* **1857**, *147* (147), 145–181. https://doi.org/10.1098/rstl.1857.0011.

(3) Anderson, M. L.; Morris, C. A.; Stroud, R. M.; Merzbacher, C. I.; Rolison, D. R. Colloidal Gold Aerogels: Preparation, Properties, and Characterization. *Langmuir* **1999**, *15* (3), 674–681. https://doi.org/10.1021/la980784i.

(4) Yeh, Y.-C.; Creran, B.; Rotello, V. M. Gold Nanoparticles : Preparation, Properties, and Applications in Bionanotechnology. *Nanoscale* **2011**, *4* (6), 1871–1880. https://doi.org/10.1039/c1nr11188d.

(5) Eustis, S.; El-Sayed, M. A. Why Gold Nanoparticles Are More Precious than Pretty Gold: Noble Metal Surface Plasmon Resonance and Its Enhancement of the Radiative and Nonradiative Properties of Nanocrystals of Different Shapes. *Chem. Soc. Rev.* **2005**, *35* (3), 209–217. https://doi.org/10.1039/b514191e.

(6) Alex, S.; Tiwari, A. Functionalized Gold Nanoparticles: Synthesis, Properties and Applications--A Review. *J Nanosci Nanotechno* **2015**, *15* (3), 1869–1894. https://doi.org/10.1166/jnn.2015.9718.

(7) Turkevich, J.; Stevenson, P. C.; Hillier, J. A Study of the Nucleation and Growth Processes in the Synthesis of Colloidal Gold. *Discuss Faraday Soc* **1951**, *11* (0), 55. https://doi.org/10.1039/df9511100055.

(8) Kimling, J.; Maier, M.; Okenve, B.; Kotaidis, V.; Ballot, H.; Plech, A. Turkevich Method for Gold Nanoparticle Synthesis Revisited. *J Phys Chem B* **2006**, *110* (32), 15700–15707. https://doi.org/10.1021/jp061667w.

(9) Brust, M.; Walker, M.; Bethell, D.; Schiffrin, D. J.; Whyman, R. Synthesis of Thiol-Derivatised Gold Nanoparticles in a Two-Phase Liquid–Liquid System. *J Chem Soc Chem Commun* **1994**, *0* (7), 801–802. https://doi.org/10.1039/c39940000801.

(10) Mackey, M. A.; Ali, M. R. K.; Austin, L. A.; Near, R. D.; El-Sayed, M. A. The Most Effective Gold Nanorod Size for Plasmonic Photothermal Therapy: Theory and In Vitro Experiments. *J Phys Chem B* **2014**, *118* (5), 1319–1326. https://doi.org/10.1021/jp409298f.

(11) Nam, J.; Won, N.; Jin, H.; Chung, H.; Kim, S. PH-Induced Aggregation of Gold Nanoparticles for Photothermal Cancer Therapy. *J Am Chem Soc* **2009**, *131* (38), 13639–13645. https://doi.org/10.1021/ja902062j.

(12) Sun, M.; Liu, F.; Zhu, Y.; Wang, W.; Hu, J.; Liu, J.; Dai, Z.; Wang, K.; Wei, Y.; Bai, J.; Gao, W. Salt-Induced Aggregation of Gold Nanoparticles for Photoacoustic Imaging and Photothermal Therapy of Cancer. *Nanoscale* **2016**, *8* (8), 4452–4457. https://doi.org/10.1039/c6nr00056h.

(13) Hong, S.; Shuford, K. L.; Park, S. Shape Transformation of Gold Nanoplates and Their Surface Plasmon Characterization: Triangular to Hexagonal Nanoplates. *Chem Mater* **2011**, *23* (8), 2011–2013. https://doi.org/10.1021/cm103273c.

(14) Nehl, C. L.; Liao, H.; Hafner, J. H. Optical Properties of Star-Shaped Gold Nanoparticles. *Nano Lett* **2006**, *6* (4), 683–688. https://doi.org/10.1021/nl052409y.

(15) Chen, J.; Wang, D.; Xi, J.; Au, L.; Siekkinen, A.; Warsen, A.; Li, Z.-Y.; Zhang, H.; Xia, Y.; Li, X. Immuno Gold Nanocages with Tailored Optical Properties for Targeted Photothermal Destruction of Cancer Cells. *Nano Lett* **2007**, *7* (5), 1318–1322. https://doi.org/10.1021/nl070345g.

(16) Nikoobakht, B.; El-Sayed, M. A. Preparation and Growth Mechanism of Gold Nanorods (NRs) Using Seed-Mediated Growth Method. *Chem Mater* **2003**, *15* (10), 1957–1962. https://doi.org/10.1021/cm020732l.

(17) Oldenburg, S. J.; Averitt, R. D.; Westcott, S. L.; Halas, N. J. Nanoengineering of Optical Resonances. *Chem Phys Lett* **1998**, *288* (2–4), 243–247. https://doi.org/10.1016/s0009-2614(98)00277-2.

(18) Zhou, H. S.; Honma, I.; Komiyama, H.; Haus, J. W. Controlled Synthesis and Quantum-Size Effect in Gold-Coated Nanoparticles. *Phys Rev B* **1994**, *50* (16), 12052–12056. https://doi.org/10.1103/physrevb.50.12052.

(19) Zhang, G.; Jasinski, J. B.; Howell, J. L.; Patel, D.; Stephens, D. P.; Gobin, A. M. Tunability and Stability of Gold Nanoparticles Obtained from Chloroauric Acid and Sodium Thiosulfate Reaction. *Nanoscale Res. Lett.* **2012**, *7* (1), 337. https://doi.org/10.1186/1556-276x-7-337.

(20) Tan, T. B.; Chu, W. C.; Yussof, N. S.; Abas, F.; Mirhosseini, H.; Cheah, Y. K.; Nehdi, I. A.; Tan, C. P. Physicochemical, Morphological and Cellular Uptake Properties of Lutein Nanodispersions Prepared by Using Surfactants with Different Stabilizing Mechanisms. *Food Funct* **2016**, *7* (4), 2043–2051. https://doi.org/10.1039/c5fo01621e.

(21) *Zeta Potential in Colloid Science - 1st Edition*. https://www.elsevier.com/books/zeta-potential-in-colloid-science/hunter/978-0-12-361961-7 (accessed 2022-07-01).

(22) Bachelet, M.; Chen, R. Self-Assembly of PEGylated Gold Nanoparticles with Satellite Structures as Seeds. *Chem Commun* **2016**, *52* (61), 9542–9545. https://doi.org/10.1039/c6cc04170a.

(23) Shan, J.; Tenhu, H. Recent Advances in Polymer Protected Gold Nanoparticles: Synthesis, Properties and Applications. *Chem Commun Camb Engl* **2007**, *0* (44), 4580–4598. https://doi.org/10.1039/b707740h.

(24) Raula, J.; Shan, J.; Nuopponen, M.; Niskanen, A.; Jiang, H.; Kauppinen, E. I.; Tenhu, H. Synthesis of Gold Nanoparticles Grafted with a Thermoresponsive Polymer by Surface-Induced Reversible-Addition-Fragmentation Chain-Transfer Polymerization. *Langmuir* **2003**, *19* (8), 3499–3504. https://doi.org/10.1021/la026872r.

(25) Bai, X.; Wang, Y.; Song, Z.; Feng, Y.; Chen, Y.; Zhang, D.; Feng, L. The Basic Properties of Gold Nanoparticles and Their Applications in Tumor Diagnosis and Treatment. *Int. J. Mol. Sci.* **2020**, *21* (7), 2480. https://doi.org/10.3390/ijms21072480.

(26) Kumari, S.; Sharma, N.; Sahi, S. V. Advances in Cancer Therapeutics: Conventional Thermal Therapy to Nanotechnology-Based Photothermal Therapy. *Pharm* **2021**, *13* (8), 1174. https://doi.org/10.3390/pharmaceutics13081174.

(27) Castano, A. P.; Demidova, T. N.; Hamblin, M. R. Mechanisms in Photodynamic Therapy: Part One—Photosensitizers, Photochemistry and Cellular Localization. *Photodiagn Photodyn* **2004**, *1* (4), 279–293. https://doi.org/10.1016/s1572-1000(05)00007-4.

(28) Mishchenko, T.; Balalaeva, I.; Gorokhova, A.; Vedunova, M.; Krysko, D. V. Which Cell Death Modality Wins the Contest for Photodynamic Therapy of Cancer? *Cell Death Dis.* **2022**, *13* (5), 455. https://doi.org/10.1038/s41419-022-04851-4.

(29) Abrahamse, H.; Kruger, C. A.; Kadanyo, S.; Mishra, A. Nanoparticles for Advanced Photodynamic Therapy of Cancer. *Photomed Laser Surg* **2017**, *35* (11), 581–588. https://doi.org/10.1089/pho.2017.4308.

(30) Huang, X.; El-Sayed, M. A. Plasmonic Photo-Thermal Therapy (PPTT). *Alex. J. Med.* **2011**, *47* (1), 1–9. https://doi.org/10.1016/j.ajme.2011.01.001.

(31) Zhang, G.; Jasinski, J. B.; Howell, J. L.; Patel, D.; Stephens, D. P.; Gobin, A. M. Tunability and Stability of Gold Nanoparticles Obtained from Chloroauric Acid and Sodium Thiosulfate Reaction. *Nanoscale Res. Lett.* **2012**, *7* (1), 337–337. https://doi.org/10.1186/1556-276x-7-337.

(32) Krainer, G.; Keller, S. Single-Experiment Displacement Assay for Quantifying High-Affinity Binding by Isothermal Titration Calorimetry. *Methods* **2015**, *76*, 116–123. https://doi.org/10.1016/j.ymeth.2014.10.034.

(33) Yoshizawa, K.; Iwahori, K.; Sugimoto, K.; Yamashita, I. Fabrication of Gold Sulfide Nanoparticles Using the Protein Cage of Apoferritin. *Chem. Lett.* **2006**, *35* (10), 1192–1193. https://doi.org/10.1246/cl.2006.1192.

(34) Tan, M. C.; Ying, J. Y.; Chow, G. M. Composition, Particle Size, and near-Infrared Irradiation Effects on Optical Properties of Au–Au2S Nanoparticles. *J. Mater. Res.* **2008**, *23* (1), 281–293. https://doi.org/10.1557/jmr.2008.0038.

(35) Bensebaa, F.; Zhou, Y.; Deslandes, Y.; Kruus, E.; Ellis, T. H. XPS Study of Metal–Sulfur Bonds in Metal–Alkanethiolate Materials. *Surface Science Letters* **1998**.

(36) Escudero, A.; Carrillo-Carrión, C.; Castillejos, M. C.; Romero-Ben, E.; Rosales-Barrios, C.; Khiar, N. Photodynamic Therapy: Photosensitizers and Nanostructures. *Mater. Chem. Front.* **2021**, *5* (10), 3788–3812. https://doi.org/10.1039/d0qm00922a.

(37) Kolarikova, M.; Hosikova, B.; Dilenko, H.; Barton-Tomankova, K.; Valkova, L.; Bajgar, R.; Malina, L.; Kolarova, H. Photodynamic Therapy: Innovative Approaches for Antibacterial and Anticancer Treatments. *Med. Res. Rev.* **2023**, *43* (4), 717–774. https://doi.org/10.1002/med.21935.

(38) Traylor, J. I.; Pernik, M. N.; Sternisha, A. C.; McBrayer, S. K.; Abdullah, K. G. Molecular and Metabolic Mechanisms Underlying Selective 5-Aminolevulinic Acid-Induced Fluorescence in Gliomas. *Cancers* **2021**, *13* (3), 580. https://doi.org/10.3390/cancers13030580.

(39) Labib, P. L.; Yaghini, E.; Davidson, B. R.; MacRobert, A. J.; Pereira, S. P. 5-Aminolevulinic Acid for Fluorescence-Guided Surgery in Pancreatic Cancer: Cellular Transport and Fluorescence Quantification Studies. *Transl. Oncol.* **2021**, *14* (1), 100886. https://doi.org/10.1016/j.tranon.2020.100886.

(40) Cornford, P. A.; Dodson, A. R.; Parsons, K. F.; Desmond, A. D.; Woolfenden, A.; Fordham, M.; Neoptolemos, J. P.; Ke, Y.; Foster, C. S. Heat Shock Protein Expression Independently Predicts Clinical Outcome in Prostate Cancer. *Cancer Res.* **2000**, *60* (24), 7099–7105.

(41) Rylander, M. N.; Feng, Y.; Zimmermann, K.; Diller, K. R. Measurement and Mathematical Modeling of Thermally Induced Injury and Heat Shock Protein Expression Kinetics in Normal and Cancerous Prostate Cells. *Int. J. Hyperth.* **2010**, *26* (8), 748–764. https://doi.org/10.3109/02656736.2010.486778.

(42) Hou, C.; Yamaguchi, S.; Ishi, Y.; Terasaka, S.; Kobayashi, H.; Motegi, H.; Hatanaka, K. C.; Houkin, K. Identification of PEPT2 as an Important Candidate Molecule in ALA-Mediated Fluorescence-Guided Surgery in WHO Grade II/III Gliomas. *J. Neuro-Oncol.* **2019**, *143* (2), 197–206. https://doi.org/10.1007/s11060-019-03158-3.

(43) Omoto, K.; Matsuda, R.; Nakai, Y.; Tatsumi, Y.; Nakazawa, T.; Tanaka, Y.; Shida, Y.; Murakami, T.; Nishimura, F.; Nakagawa, I.; Motoyama, Y.; Nakamura, M.; Fujimoto, K.; Hiroyuki, N. Expression of Peptide Transporter 1 Has a Positive Correlation in Protoporphyrin IX Accumulation Induced by 5-Aminolevulinic Acid with Photodynamic Detection of Non-Small Cell Lung Cancer and Metastatic Brain Tumor Specimens Originating from Non-Small Cell Lung Cancer. *Photodiagnosis Photodyn. Ther.* **2019**, *25*, 309–316. https://doi.org/10.1016/j.pdpdt.2019.01.009.

(44) Younus, L. A.; Mahmoud, Z. H.; Hamza, A. A.; Alaziz, K. M. A.; Ali, M. L.; Yasin, Y.; Jihad, W. S.; Rasheed, T.; Alkhawaldeh, A. K.; Ali, F. K.; Kianfar, E. Photodynamic Therapy in Cancer Treatment: Properties and Applications in Nanoparticles. *Braz. J. Biol.* **2024**, *84*, e268892. https://doi.org/10.1590/1519-6984.268892.

(45) Jayakumar, S.; Kunwar, A.; Sandur, S. K.; Pandey, B. N.; Chaubey, R. C. Differential Response of DU145 and PC3 Prostate Cancer Cells to Ionizing Radiation: Role of Reactive Oxygen Species, GSH and Nrf2 in Radiosensitivity. *Biochim. Biophys. Acta (BBA) - Gen. Subj.* **2014**, *1840* (1), 485–494. https://doi.org/10.1016/j.bbagen.2013.10.006.